Check for updates

ORIGINAL RESEARCH

Molecular Features and Stages of Pulmonary Fibrosis Driven by Type 2 Inflammation

Hamid Mattoo[1]*, Dinesh S. Bangari[3], Sheila Cummings[3], Zachary Humulock[2], David Habiel[2], Ethan Y. Xu[1,6], Nathan Pate[3], Robert Resnick[2], Virginia Savova[1], George Qian[2], Christian Beil[5], Ercole Rao[5], Frank O. Nestle[2], Paul J. Bryce[2], and Arun Subramaniam[4]*

[1]Precision Medicine and Computational Biology, [2]Immunology and Inflammation Research Therapeutic Area, [3]Discovery Pathology, Translational In Vivo Models Platform, and [4]US Medical Affairs, Sanofi, Cambridge, Massachusetts; [5]Biologics Research, Sanofi, Frankfurt, Germany; and [6]Aspen Neuroscience, San Diego, California

Abstract

Systemic sclerosis (SSc) is a progressive, multiorgan disease with limited treatment options. Although a recent proof-of-concept study using romilkimab or SAR156597, a bispecific IL-4/IL-13 antibody, suggests a direct role of these cytokines in the pathophysiology of SSc, their contributions to the balance between inflammation and fibrosis are unclear. Here, we determine the roles of type 2 inflammation in fibrogenesis using FRA2-Tg (Fos-related antigen 2–overexpressing transgenic) mice, which develop spontaneous, age-dependent progressive lung fibrosis. We defined the molecular signatures of inflammation and fibrosis at three key stages in disease progression, corresponding to preonset, inflammatory dominant, and fibrosis dominant biology, and revealed an early increase in cytokine–cytokine receptor interactions and antigen-processing and presentation pathways followed by enhanced Th2- and M2 macrophage–driven type 2 responses. This type 2 inflammation progressed to extensive fibrotic pathology by 14–18 weeks of age, with these gene signatures overlapping significantly with those seen in the lungs of patients with SSc with interstitial lung disease (ILD). These changes were also evident in the histopathology, which showed perivascular and peribronchiolar inflammation with prominent eosinophilia and accumulation of profibrotic M2-like macrophages followed by rapid progression to fibrosis with thickened alveolar walls with multifocal fibrotic bands and signs of interstitial pneumonia. Critically, treatment with a bispecific antibody targeting IL-4 and IL-13 during the inflammatory phase abrogated the Th2 and M2 responses and led to near-complete abrogation of lung fibrosis. These data recapitulate important features of fibrotic progression in the lungs of patients with SSc-ILD and enhance our understanding of the progressive pathobiology of SSc. This study also further establishes FRA2-Tg mice as a valuable tool for testing future therapeutic agents in SSc-ILD.

Keywords: systemic sclerosis; interstitial lung disease; IL-4; IL-13; fibrosis

Accumulation of extracellular matrix (ECM) and excessive tissue scarring after tissue injury and the replacement of functional microcosms of cells and interstitia with collagen-rich scar are hallmarks of pathogenic fibrosis and result in defective organ function. The initiating tissue damage trigger in many fibrotic responses can result from genetic, environmental, or pathogenic distress but is accompanied by an inflammatory response enriched in type 2 cells, including T-helper cell type 2 (Th2) cells, M2 macrophages, eosinophils, and mast cells (1). Such responses are observed in several chronic human immune-mediated diseases, including asthma, systemic sclerosis (SSc), interstitial lung disease (ILD), and ulcerative colitis (2–4), with M2-like and monocyte-derived macrophages having key roles in lung, liver, and skin fibrosis (2) and $SPP1^{+}$ macrophages, which resemble M2-polarized macrophages, found in the lungs of patients with idiopathic pulmonary fibrosis (IPF) (5). However, despite extensive

(Received in original form August 3, 2022; accepted in final form June 27, 2023)

*Co–senior authors.

Author Contributions: Conceptualization: H.M. and A.S. Methodology: H.M., D.S.B., S.C., Z.H., N.P., R.R., V.S., G.Q., C.B., and E.R. Formal analysis: H.M., D.S.B., S.C., D.H., Z.H., E.Y.X., and N.P. Investigation: H.M., A.S., D.S.B., D.H., and P.J.B. Resources: A.S., P.J.B., F.O.N., and V.S. Writing of the original draft: H.M. and A.S. Writing, review, and editing: P.J.B., D.H., D.S.B., and F.O.N. Supervision: A.S., H.M., and P.J.B. Visualization: H.M., D.S.B., and S.C.

Correspondence and requests for reprints should be addressed to Arun Subramaniam, Ph.D., 450 Water Street, Cambridge, MA. E-mail: Arun.subramaniam@sanofi.com and Hamid Mattoo, Ph.D., 350 Water Street, 8th floor, 02141 Cambridge, MA. E-mail: hamid.mattoo@sanofi.com.

This article has a related editorial.

This article has a data supplement, which is accessible from this issue's table of contents at www.atsjournals.org.

Am J Respir Cell Mol Biol Vol 69, Iss 4, pp 404–421, October 2023
Copyright © 2023 by the American Thoracic Society
Originally Published in Press as DOI: 10.1165/rcmb.2022-0301OC on June 27, 2023
Internet address: www.atsjournals.org

Clinical Relevance

This study provides a temporal analysis of evolution of sustained inflammation into progressive tissue remodeling. This study also provides molecular evidence for role of IL-4 and IL-13 in SSc-ILD pathogenesis, as observed clinically in a Phase 2 clinical study of the bi-specific IL-4/IL-13 antibody. In addition, the study provides further evidence for using FRA2-Transgenic mice as a model of lung fibrosis observed in systemic sclerosis.

research efforts and delineation of various pathogenic pathways using a combination of preclinical models and *in vitro* research, identification of effective therapeutic targets has been extremely difficult. A better understanding of fibrotic mechanisms in human tissues can be achieved by incorporating preclinical studies with information derived from the vast collection of human tissue–derived datasets available in the public domain, and it could facilitate the development of effective therapies.

SSc is an orphan disease with very limited therapeutic options (6). With progressive thickening and fibrosis characterized by excessive ECM deposition and tissue remodeling, seen in almost all major internal organs, SSc often presents with ILD and nonspecific interstitial pneumonia, which is the cause of more than half of the disease-related mortality (6). Although type 2 inflammation has been implicated as a mediator of fibrosis of the skin and lung in SSc (7, 8), this has hinged mainly on association with type 2 biomarkers such as increased periostin and buildup of IL-4– and IL-13–related pathways (9). However, a recent clinical trial using SAR156597, a bispecific antibody targeting IL-4 and IL-13, showed efficacy in reducing the modified Rodnan skin score and a nonsignificant but favorable effect on lung outcomes at Week 24 (10) and demonstrated a beneficial effect of inhibiting IL-4 and IL-13 as a disease-modifying agent in scleroderma.

To examine the roles that IL-4 and IL-13 might play in the complex processes of initiation, inflammation, and fibrosis, we used mice overexpressing FRA-2 (Fos-related antigen 2), a murine model for SSc-related pulmonary fibrosis and hypertension (11). We and others have previously demonstrated that FRA-2–transgenic (FRA-2-Tg) mice spontaneously develop pulmonary inflammation as well as vascular and parenchymal remodeling, features characteristic of patients with SSc with pulmonary involvement (11–14). This model facilitated a detailed analysis of the progressive evolution of inflammatory fibrosis of the lung with a transcriptomic and phenotypic snapshot of different stages of the disease that ultimately manifest in a fibrotic lung. This study takes a systems biology approach to integrate these findings into studies in the lungs and skin of patients with SSc.

The experiments in this study define the development and progression of type 2 inflammation into a dominant profibrotic pathway and capture the molecular consequences of therapeutic intervention with antibody blockage. These findings demonstrate a significant overlap with available data from the lungs of patients with SSc, thus highlighting the potential therapeutic value of this pathway in SSc-ILD.

Methods

Animal Experiments

Female FRA-2 TG mice and wild-type (WT) littermates were bred in the vivarium located at The Jackson Laboratory and transferred to the Sanofi vivarium and used in studies after an acclimatization period. Mice were maintained under specific pathogen-free conditions in isolated ventilated cages with 12-h/12-h light/dark cycles. All animal experiments met institutional animal care and use committee guidelines and were approved by the local authorities.

Public Gene Expression Data

The Gene Expression Omnibus (https://www.ncbi.nlm.nih.gov/geo/) database was queried for gene expression datasets including SSc with ILD (15), and appropriate datasets containing patient and control samples were selected. In addition, only patients with SSc who had received no treatment were included. We identified two lung datasets for lung tissue (accession numbers GSE48149 and GSE76808). The selected datasets comprised 27 samples (16 cases and 11 controls).

Histologic and Immunohistochemical Methods and Pathologic Analysis

At necropsy, lungs were collected and inflated with and then placed in 10% neutral-buffered formalin. After fixation, tissues were subjected to routine histologic processing, embedded in paraffin, cut at 5 μm, and stained with hematoxylin and eosin. In addition, lungs were stained using Masson's trichrome for detection of fibrosis (trichrome stain kit; Roche Diagnostics). Lungs were semiquantitatively scored for fibrosis, overall inflammation, and eosinophil density by a board-certified pathologist in a blinded manner. FRA2 immunohistochemistry (IHC) was performed using anti-FRA2 monoclonal antibody (Millipore catalog no. MABS1261; clone REY146C). For arginase IHC, unstained sections were subjected to immunostaining using rabbit antiarginase polyclonal antibody (catalog no. ab96183; Abcam) using the Bond Polymer Refine kit in the BondRX automated immunostaining platform (Leica Biosystems). Pathology and IHC grading criteria were as follows:

- *Overall inflammation*: 0 (no pathology); 1 (minimal pathology; perivascular/peribronchiolar inflammatory infiltrate is slightly increased); 2 (mild pathology; perivascular/peribronchiolar inflammatory infiltrate is present around some of the vasculature and bronchioles with only very minimal interstitial involvement); 3 (moderate pathology; inflammatory infiltrate is present around most of the vasculature and bronchioles and extends into the interstitia); 4 (severe; inflammatory infiltrate extends into the surrounding interstitia and forms coalescing foci)
- *Eosinophil density*: 0 (none); 1 (minimal; few scattered eosinophils are present in inflammatory infiltrate); 2 (mild; more numerous eosinophils scattered throughout the inflammatory infiltrate); 3 (moderate; numerous eosinophils compose the inflammatory infiltrate, forming clusters); 4 (severe; eosinophils form coalescing clusters or dominate the population of inflammatory cells)
- *Pulmonary fibrosis*: 1 (normal lung); 2 (minimal fibrous thickening of alveolar or bronchiolar walls); 2 (moderate thickening of walls without obvious damage to lung architecture); 3 (increased fibrosis with definite

damage to lung structure and formation of fibrous bands or small fibrous masses); 4 (severe distortion of structure and large fibrous areas)

Antiarginase IHC scores were as follows: 0 (no immunoreactive cells present); 1 (scattered immunoreactive cells present); 2 (more noticeable numbers of immunoreactive and larger cells); 3 (clusters of immunoreactive cells multifocally present); 4 (coalescing clusters of immunoreactive cells throughout most of the section).

In quantitative analysis for trichrome-stained area in the lung, whole-slide images of Masson's trichrome–stained mouse lungs were analyzed using an algorithm to detect stained area using Visiopharm image analysis software (version 2022.01). A deep learning–based automated tissue classification solution was developed to detect lung parenchyma (alveoli) while excluding large airway lumen, bronchiolar mucosal epithelium, and large blood vessels. Blue-stained areas within the lung were then automatically detected and quantitated as the trichrome-positive area (indicative of collagen) presented as a percentage of the total tissue area.

Tissue Processing and RNA Extraction

All tissue samples from mouse lungs were harvested in RNAlater. Tissue samples were transferred to Matrix A tubes containing 1 ml of buffer RLT with 2-mercaptoethanol and homogenized in MP Biomedicals homogenizer using program 1 (two 40-s cycles separated by 5 min to avoid sample heatup). Matrix A tubes were then spun at 10,000 × *g* for 3 minutes. We then collected 350 μl of lysate (in 1% vol/vol buffer RLT with 2-mercaptoethanol). A pipette with a multichannel was used multiple times (∼20 times) to lyse the cells. RNA was prepared using the RNeasy 96 QIAcube HT kit (Qiagen, Hilden, Germany). The protocol was modified from the Qiagen version as detailed in the data supplement.

RNA-Sequencing Library Preparation, Sequencing, and Data Processing

First-strand cDNA synthesis was performed with 500 ng of total RNA for the RNA-sequencing (RNA-seq) workflow. For first-strand cDNA synthesis, anchored oligo(dT) and SuperScript III were used (Thermo Fisher Scientific). This was followed by second-strand cDNA synthesis, which was performed using RNase H, DNA polymerase I, and the provided second-strand buffer. For the purification of double-stranded cDNA, DNA Clean and Concentrator-5 (Zymo Research) was used. The Nextera XT DNA Library Preparation Kit (Illumina) was used for library preparation. Agencourt AMPure XP beads were used for cleaning the prepared libraries according to the manufacturer's instructions (Beckman Coulter). The quality and fragment size of the prepared libraries were evaluated by using the High Sensitivity DNA Kit on the 2100 Bioanalyzer (Agilent). The libraries from multiple samples were multiplexed, pooled, and sequenced on an Illumina HiSeq with 50-bp paired-end reads. Sequencing reads were aligned to National Center for Biotechnology Information build 37.2 using TopHat (version 2.1.0) (16). For quantifying the expression levels and calculating normalized fragments per kilobase of transcript per million mapped reads values, Cuffquant and Cuffnorm (Cufflinks version 2.2.1) were used (17). Fastq files were uploaded to Qiagen Array Studio, and samples were processed on OmicSoft software.

10x Genomics 5′ Gene Expression Profiling

Samples were processed as per the Chromium Single Cell V2 Reagent Kits Protocol by 10x Genomics. Approximately 6,000–8,000 cells were targeted for each sample recovery. Cells were first stained with Fc block followed by CD45 antibody for 30 minutes on ice. Cells were then labeled with DAPI to identify and exclude dead cells, and viable cells were sorted using the BD FACSAria device into RPMI-10 with 1% FBS. Cells were spun at 500 × *g* for 5 minutes (at 4°C) and processed for 10x droplet and library generation using the protocol provided by 10x Genomics (https://www.10xgenomics.com/support/user-guides/single-cell-gene-expression?menu%5BproductNames%5D%5B0%5D=Single%20Cell%20Gene%20Expression). The 2100 Bioanalyzer instrument (Agilent) using the high-sensitivity DNA Chips and Kit (Agilent catalog no. 5067-4626) was used to assess the quality and quantity of cDNA and end libraries. Real-time quantitative PCR (qPCR) was performed for a more accurate quantification of libraries after serial dilution of the libraries at 1:100,000, 1:200,000, 1:400,000, and 1:800,000 in 10 mM Tris-HCl. The Kapa Library quantification kit (Kapa Biosystems, catalog no. KK4824-07960140,001) was used for qPCR on the QuantStudio 7 Flex Real-Time PCR system. The qPCR cycling protocol was performed as per the protocol provided in the Kapa Library quantification kit (14). Libraries were pooled at equimolar concentrations to obtain a final library pool at a concentration of 2 nM. Sequencing was performed on the NovaSeq 6000 system (Illumina) with the NovaSeq 6000 S1 Reagent Kit (300 cycles) (catalog no. 20012863). Sequencing depth and cycle number were as per the 10x Genomics recommendations. For 3′ (V2) gene expression libraries, read 1 was 26 cycles, i7 index was 8 cycles, and read 2 was 98 cycles. Sequencing was performed at 2–30,000 read pairs per cell.

Single-Cell Data Analysis

After BCL conversion, CellRanger Pipeline (10x Genomics) was used to process the fastq files, resulting in demultiplexing, transcript alignment, read filtering, barcode quantification, and unique molecular identifier counting and generating matrices of cells × barcodes. These matrices were then uploaded into the SPRING portal (18), which is an interactive tool for visualizing and analyzing single-cell data (19). Using this, the single-cell data obtained from whole lungs of FRA2-Tg and WT mice were visualized and analyzed for cell type–specific changes. The Gene-Finder tool was used to identify cells expressing genes of interest and compare across groups. Analysis of differentially expressed genes (DEGs) was performed with the R package Seurat17 (version 3.0.0) with the FindMarkers function using the default settings.

ELISA

For the albumin ELISA, frozen BAL fluid supernatants were thawed on ice. BAL fluid supernatants were diluted 1:10,000 in the dilution buffer supplied with the albumin ELISA kit (Bethyl Laboratories, catalog no. E99-134). For the autoantibody ELISAs, frozen serum was thawed on ice and diluted 1:100 in the dilution buffer supplied with the mouse anti-SCL-70 ELISA kit (Signosis, catalog no. EA-5205) and the mouse anti-JO-1 ELISA kit (Signosis, catalog no. EA-5207). Diluted sample (100 μl) or standard curve was added to the kit-provided plates and incubated for 1 hour at room temperature. Plates were washed. A quantity of 100 μl of antialbumin detection antibody or IgG

Table 1. Upstream Regulators Modulating Gene Expression Patterns in Systemic Sclerosis and Interstitial Lung Disease

Upstream Regulator	Molecule Type	Activation *z*-Score	*P* Value of Overlap
TGFB1	Growth factor	4.545	9.12E-52
FGF2	Growth factor	3.034	1.22E-15
AGT	Growth factor	2.997	5.1E-20
IGF1	Growth factor	2.577	9.95E-17
HGF	Growth factor	2.476	3.67E-16
TNF	Cytokine	5.986	7.55E-60
OSM	Cytokine	4.808	4.9E-23
IFNG	Cytokine	4.633	9.26E-28
IL1B	Cytokine	4.292	6.28E-27
IL1A	Cytokine	4.018	1.13E-14
CSF2	Cytokine	3.86	6.03E-17
IL6	Cytokine	3.752	5.87E-22
IL5	Cytokine	2.372	6.05E-14
IL13	Cytokine	2.116	1.1E-23
IL17A	Cytokine	1.823	4.01E-19
IL4	Cytokine	1.69	6.39E-19
WNT3A	Cytokine	1.543	7.32E-17
IL33	Cytokine	1.523	3.09E-12

Analyzed GSE48149 for upstream regulators and compared systemic sclerosis and idiopathic pulmonary fibrosis (SSc-IPF) with SSc with pulmonary artery hypertension (SSc-PAH), two independent disease states that present with pulmonary fibrosis and PAH. Upstream regulator analysis of cytokines and growth factors among differentially expressed genes in SSc-PAH and SSc-IPF. Data are represented as *z*-scores, and *P* values are mentioned in the last column.

horseradish peroxidase antibody for autoantibody kits was added to wells and incubated for either 1 hour for the albumin ELISA or 30 minutes for the autoantibody ELISA at room temperature. Plates were washed. A quantity of 100 μl of tetramethylbenzidine substrate was added to each well and incubated for 30 minutes at room temperature. A quantity of 50 μl of stop solution was added to each well. Absorbance at 450 nm was read for the plate using the SpectraMax M5e plate reader.

Flow Cytometry, Staining, and Analysis

BD LSR Fortessa (five lasers) and Bio-Rad ZE5 analyzers were used for all flow cytometry experiments. Compensation was performed before assay setup on the flow cytometer using a standard procedure. For cell surface staining, cell centrifugation was performed at 300 × *g* at 12°C for 5 minutes. Supernatants were discarded, and 100 μl of the staining panel with selected antibody cocktails (supplementary information) was added to each cell pellet, and cells were resuspended and allowed to incubate on ice in the dark for 30–45 minutes. After this step, cell centrifugation was performed as above, supernatants were discarded, and cell pellets were resuspended in 200 μl of blue viability dye (1 μl of 7-aminoactinomycin D with 999 μl of staining buffer) and incubated at room temperature for 10 minutes in the dark. This was followed by sample washing with phosphate buffered saline (PBS) as described above and readied for acquisition on the cytometer. All flow analysis was performed using FlowJo version 10. For detailed information on flow analysis, please refer to the data supplement.

Methods of Pathway Analysis

Pathway analysis was performed using Ingenuity Pathway Analysis (IPA) (Qiagen). Transcripts that were identified to be differentially expressed during the timed series developmental study of lungs between FRA2-Tg and WT mice with a greater than twofold change and a *P* value less than 0.05 were input into IPA bioinformatic analysis using gene identifiers. Similar thresholds were used for analysis of public transcriptomic data from human diseases. Differentially expressed transcripts were analyzed in IPA using core analysis followed by a comparison analysis between each time point in the case of the lung developmental study and between different groups in the case of the study using monoclonal antibody treatments. Datasets were assessed for prediction of canonical pathways and upstream regulators. In addition, signatures were curated from public datasets from lung samples of patients with SSc and patients with IPF from the GSE48149, GSE76808, GSE81292, GSE53845, GSE24206, GSE10667, GSE101286, and GSE47460 datasets, as well as two meta-analyses performed on SSc and IPF samples, respectively (20, 21).

Results

IL-4 and IL-13 Are Upstream Regulators in SSc-ILD Lungs

To identify potential pathways responsible for regulating pathology in SSc-ILD lungs, gene expression datasets from SSc-ILD lungs were identified (GSE48149 and GSE76808) (19, 22), and raw data were processed for DEGs, considered to be those displaying a >1.5-fold change difference and with an adjusted *P* value <0.05. These DEGs were then queried for canonical pathway analysis and upstream regulator analysis using IPA, with a focus on cytokines and growth factors. Among the major growth factors that modulated the DEG profiles were transforming growth factor-β1 (TGFB1), epidermal growth factor, vascular endothelial growth factor A, and fibroblast growth factor 2 (*see* Supplementary Data File E1 in the data supplement), a finding consistent with the fibrotic phenotype of the lung observed in these patients. The major cytokines modulating the gene expression include TNF, IFNG, IL-1B, and colony-stimulating factor 2 (CSF2) and crucially also key type 2 inflammatory mediators, including IL-4, IL-13, IL-5, and IL-33 (Table 1).

A comparison between SSc-ILD and the other inflammatory/fibrotic conditions reveals a conserved set of upstream regulators, such as TNF, TGFB1, SREBF2 (sterol regulatory element binding transcription factor 2), IL-1B, and CSF2 (Table E1 and Supplementary Data File E1). In addition to this core set of potentially pathogenic molecules, certain modulators specific to a subset of conditions could also be identified. The type 2 inflammatory response modulated by IL-4, IL-13, IL-5, and IL-33 is enriched in SSc-ILD and IPF compared with idiopathic pulmonary arterial hypertension (Table E1). These results demonstrate that molecular signatures of the type 2 cytokine pathways are overexpressed in the lungs of patients with SSc-ILD. To expand on the role of type 2 inflammation in SSc-ILD pathogenesis, we performed detailed studies in the FRA2-Tg mouse, which has

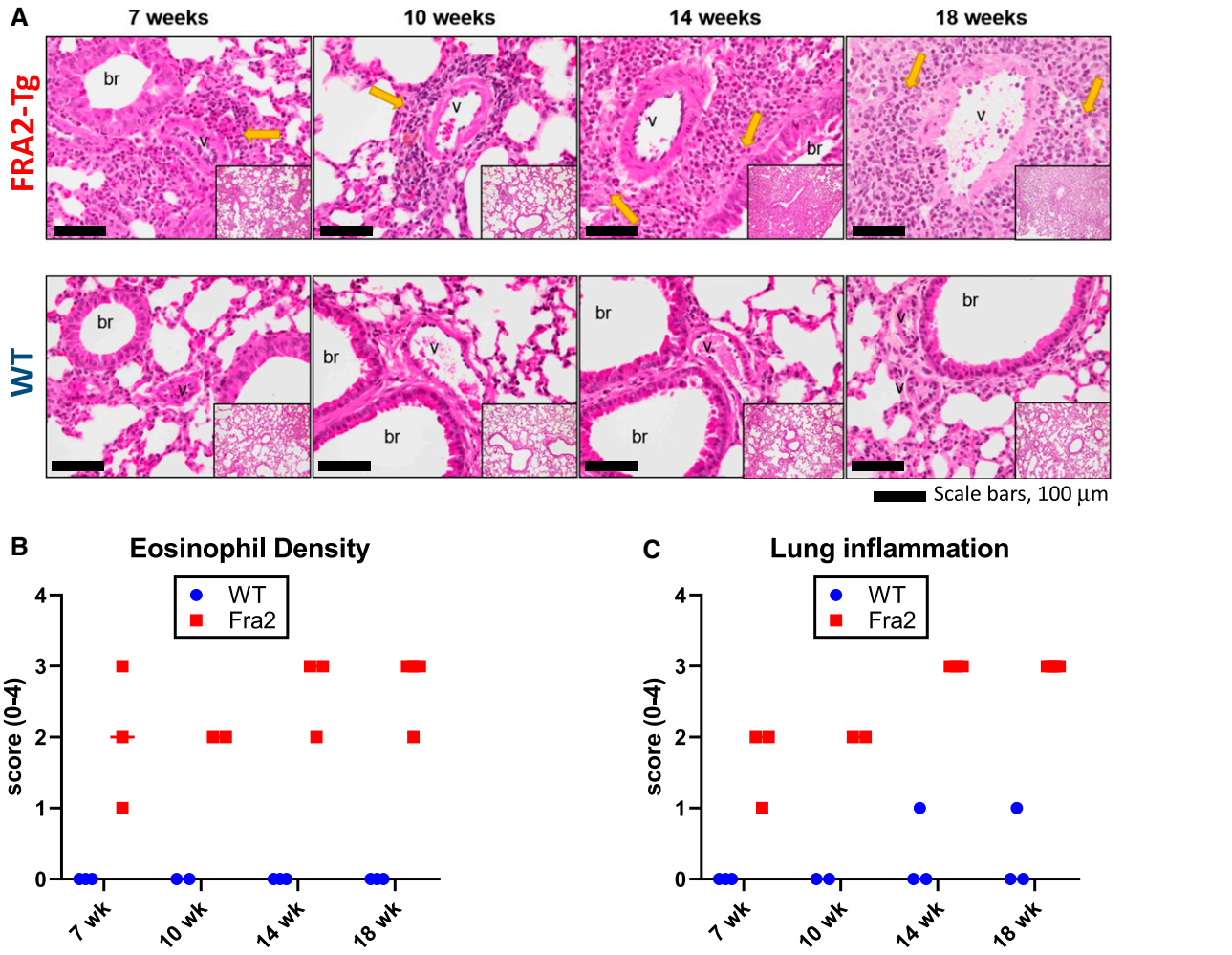

Figure 1. Progression of inflammation in Fos-related antigen 2–overexpressing transgenic (FRA2-Tg) lungs with age. (*A*) Representative images of hematoxylin and eosin–stained lungs from FRA2-Tg mice (top row) depicting perivascular (v) and peribronchiolar (br) inflammatory infiltrate composed of eosinophils (arrows) and mononuclear cells. Bottom row images depict age- and sex-matched wild-type (WT) control animals. Images magnified at 400×. Insets magnified at 100×. Scale bars, 100 μm. (*B*) Scatter dot plots of eosinophil density score. (*C*) Scatter dot plots of total inflammation score. br = bronchiole; v = vessel.

been shown to develop a spontaneous, robust type 2 peribronchiolar inflammation and progressive age-dependent lung remodeling and fibrosis (23, 24).

Investigating the Stages of Lung Inflammation and Tissue Remodeling in the FRA2-Tg Mouse Model

Prior reports have described similarities between the FRA2-Tg lungs and SSC-diseased lungs (24, 25), and we performed a detailed temporal analysis to better understand the evolution of the pathogenic lung disease. FRA2-Tg mice were generated on the basis of a prior report (11), and strain 902 was chosen because it incorporated four copies of the FRA2 (*Fosl2*) transgene, as previously used (11) (Figure E1). These mice showed progressive lung pathology, including increased lung weight and progressively increasing hydroxyproline content (Figures E2A and E2B). To assess the lung pathology in an age-dependent way, we initially performed a detailed histological analysis for inflammation using hematoxylin and eosin staining. Leukocyte infiltration was seen as early as 7 weeks of age (Figure 1A), but the lung morphology was mostly intact with visibly functional bronchioles and vessels. In contrast, by 14 weeks, the inflammation was very aggressive, with a perivascular and peribronchiolar pattern (Figure 1A). The first apparent pathological alteration involved obliteration of pulmonary arteries. This frequently coincided with perivascular inflammation in the absence of altered bronchial architecture. Pulmonary arterial wall thickening was observed at 10 weeks of age and preceded the onset of fibrosis by 2–4 weeks. The immune infiltrate is composed of macrophages, eosinophils, lymphocytes, some plasma cells, and neutrophils, which often extend to surrounding interstitia.

FRA2 overexpression was demonstrated via IHC in a variety of cell types in the lung tissue of FRA2-Tg mice (Figures E3A and E3B). Compared with 16-week-old WT (C57BL/6) mice, age-matched FRA2-Tg mice revealed a prominent nuclear IHC signal indicative of FRA2 overexpression in airway and bronchial epithelial cells, vascular endothelial cells, fibroblasts, mononuclear cells (lymphocytes and macrophages), and

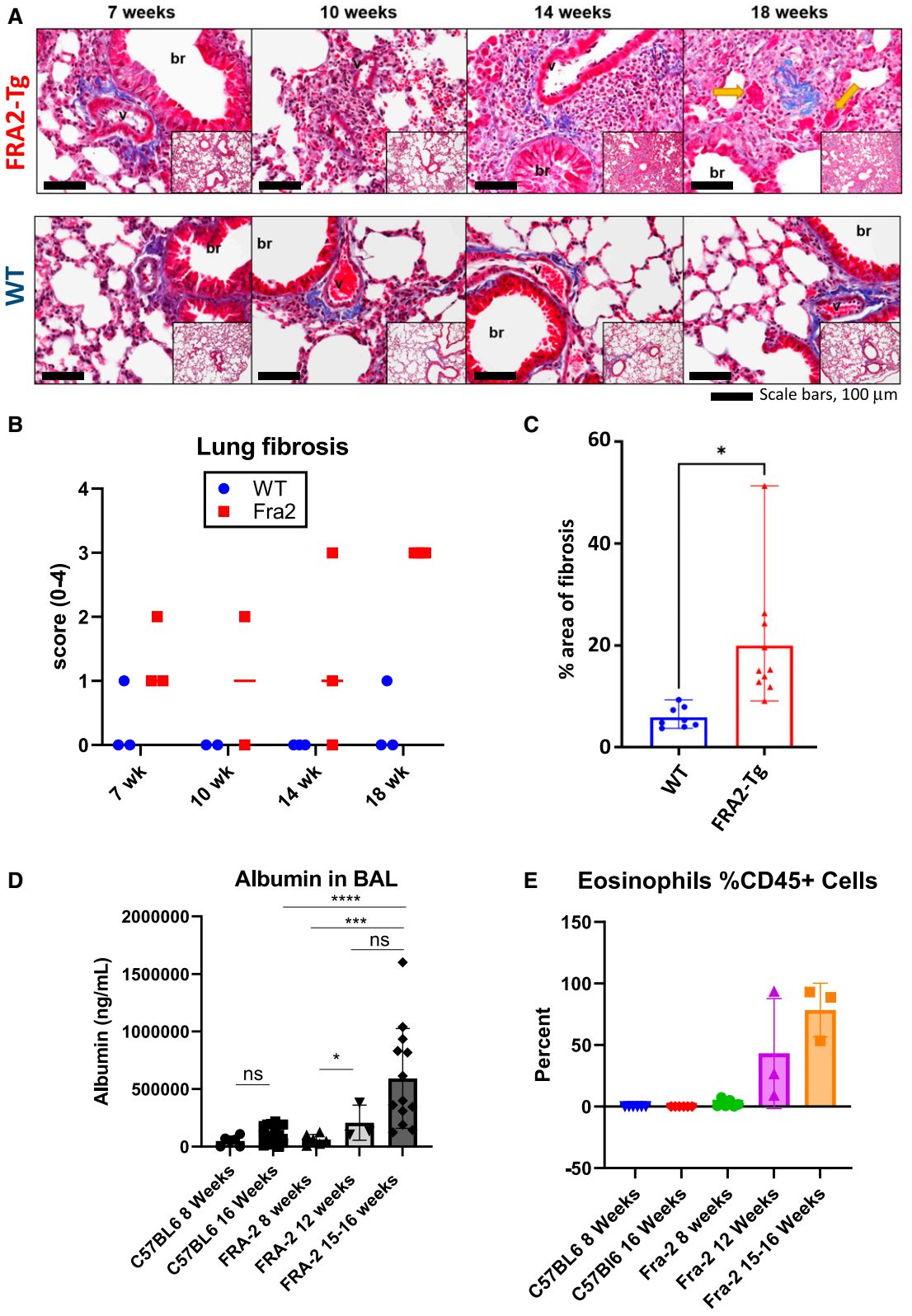

Figure 2. Progression of fibrosis in FRA2-Tg lungs with age. (*A*) Representative images of Masson trichrome–stained lungs from FRA2-Tg mice (top row). Increased blue staining of fibrous connective tissue is appreciable at 18 weeks with thickening alveolar walls and formation of fibrous bands multifocally. Bottom row depicts age- and sex-matched WT littermate control animals in which all depicted lungs express a normal

polymorphonuclear cells (eosinophils and neutrophils). In addition, chondrocytes in the tracheal cartilage and adipocytes of the mediastinal brown fat revealed FRA2 overexpression compared with WT mice. A strong FRA2 signal was detected in eosinophils that were also the most prominent cell types within the inflammatory infiltrates of the FRA2-Tg mice. Using single-cell RNA-seq data from the lungs of patients with SSc-ILD (26), the *FRA2* gene is expressed predominantly in mesenchymal cells (fibroblasts), epithelial cell subsets, endothelial cells, and immune cells such as myeloid cells, mast cells, natural killer (NK)/T cells, and plasmablasts. Interestingly, levels of *FRA2* transcripts are elevated in the fibroblasts of patients with SSc-ILD compared with those of healthy control subjects (Figure E4).

Eosinophilic inflammation has been projected as one pathogenic mechanism in SSc (27). Eosinophils tend to accumulate in mouse lungs as eosinophilic crystalline pneumonia (ECP) (28), which is characterized by numerous large eosinophilic macrophages and multinucleated giant cells admixed with eosinophils, neutrophils, and, in some cases, lymphocytes and plasma cells within alveolar spaces that multifocally obscure normal pulmonary architecture (shown as arrows in Figure 1A). Eosinophil levels are depicted as eosinophil density score and are elevated in the lungs of all the FRA2-Tg animals at all ages compared with WT littermate control animals (Figure 1B). The lung inflammation is quantified in Figure 1C and is visibly very progressive in FRA2-Tg mice, and it reaches the peak by the last time point analyzed at 18 weeks of age.

ECP starts appearing in FRA2-Tg lungs at 14 weeks but is very prominent at Week 18 (Figure 2A, yellow arrows). Mice had to be killed by Weeks 19 and 20 because of debilitating comorbidities of lung, liver, and skin fibrosis and visible distress. Lung fibrosis was visibly more distinct in the lungs of FRA2-Tg animals, surrounding the vasculature and bronchioles, expanding into the interstitia, and multifocally thickening alveolar septae (Figures 2A and E5). Occasionally, bands of fibrosis were observed within regions of inflammatory infiltrate, and fibroblastic foci were also visible. The extent of fibrosis was significantly more abundant in the lungs of FRA2-Tg animals than in those of WT control animals using both a pathology score and digital quantification (Figures 2B and 2C). These data establish the progression of spontaneous type 2 inflammation and tissue remodeling in the lungs of FRA2-Tg animals.

Interestingly, this progressive inflammation and fibrosis is associated with a decrease in epithelial barrier integrity evident through a progressive increase of BAL albumin levels of FRA2-Tg animals with age, whereas no such increase was observed in WT littermate control animals (29) (Figure 2D). This defective barrier was observed with an early influx of neutrophils in 8-week-old animals and a progressive influx of eosinophils and monocytes in BAL, with the former making up a majority of cells and a progressive decline in alveolar macrophages (Figures 2E and E6A–E6C). No difference in total CD4 T cells or dendritic cells (DCs) was observed (Figures E6D and E6E). These data suggest that FRA2-Tg animals have progressive defects in lung epithelial barrier function and eosinophilic inflammation as they age.

Molecular Features Characterizing Stages of Type 2 Inflammation–driven Pulmonary Fibrosis

We next sought to investigate changes in the molecular patterns over age to capture the sequence of events that leads to the pathogenic inflammation and fibrosis in the lungs in FRA2-Tg mice. Lungs were harvested from FRA2-Tg and WT littermate animals at 4, 7, 10, 14, and 18 weeks of age, and whole-transcriptome analysis was performed (Figure 3A). Principal component analysis of this time-series analysis revealed a progressive change in the global transcriptome of lungs from FRA2-Tg animals compared with the WT littermate control animals, which show minimal changes with age (Figure 3B). Minimal changes in WT animals over 14 weeks (Weeks 4 to 18) are consistent with a recent report describing disrepair in aging lungs of 52–72-week-old animals, but no significant differences were observed during the first 20 weeks (30). In contrast, lungs from FRA2-Tg mice showed a progressive global shift of transcriptomic features over time, consistent with the histopathological changes observed. The number of DEGs ($P < 0.01$; Log_2 fold change, >1.5) was small at 4 weeks but included secreted inflammatory mediators such as *Csf2* and *Cxcl12*. The numbers of DEGs progressively increased at 7, 10, 14, and 18 weeks of age (Figures 3C and E7), with many inflammatory mediators being elevated by 7 weeks of age in FRA2-Tg lungs and increasingly elevated up to the 18-week time point.

The top DEGs were divided into biological categories and compared across the two genotypes across all the time points (Figure E7). Comparing DEGs across different time points, pathway analyses revealed a developing T cell–driven response with enrichment of Th2 and Th17 pathways. In addition, there was a very strong enrichment of chemokine signaling and DC maturation, leukocyte extravasation, and fibrosis pathways (Figure 3D, left panel). Analysis of the gene expression hierarchy was performed by looking for enrichment of upstream regulators, and a number of Th1 and Th17 cytokines and alarmins (IFNG, IL-4, IL-13, IL-5, TSLP, OSM, IL-33, IL-17A) as well as other inflammatory cytokines, including IL-6, IL-18, and IL-1B, were progressively enriched in the lungs of FRA2-Tg animals with advancing age (Figure 3D, right panel). The enrichment of the Th2 signature was especially strong, as shown by enhanced expression of genes associated with eosinophil adhesion and migration, IL-4–responsive genes, as well as IL-9 signaling and M2 macrophage pathways (Figure 3E). Cell-type deconvolution of the immune infiltrate using gene signatures derived from a recent single-cell RNA-seq study in murine lungs (31, 32) was performed (Figure E8), and the findings supported a progressing inflammation dominated by accumulation of inflammatory monocytes, macrophages, and DCs and a robust $CD4^+$ T cell–driven response. Also, signatures of eosinophil and neutrophil

Figure 2. (*Continued*). amount of blue-stained fibrous connective tissue. (*B*) Scatter dot plots of total fibrosis score. Scores were as assigned by the expert pathologist; age of animals is shown on *x*-axis. Data are represented as the mean of multiple replicates. Scale bars, 100 μm. (*C*) Quantification of Masson trichrome staining (error bars represent mean ± SE; $^*P < 0.05$). (*D*) Quantified BAL albumin levels from WT and FRA2-Tg animals at different ages using ELISA (error bars represent mean ± SE; $^{***}P < 0.001$ and $^{****}P < 0.0001$). (*E*) Frequency of eosinophils depicted as a percentage among $CD45^+$ gated cells from lungs of WT and FRA2-Tg animals at different ages.

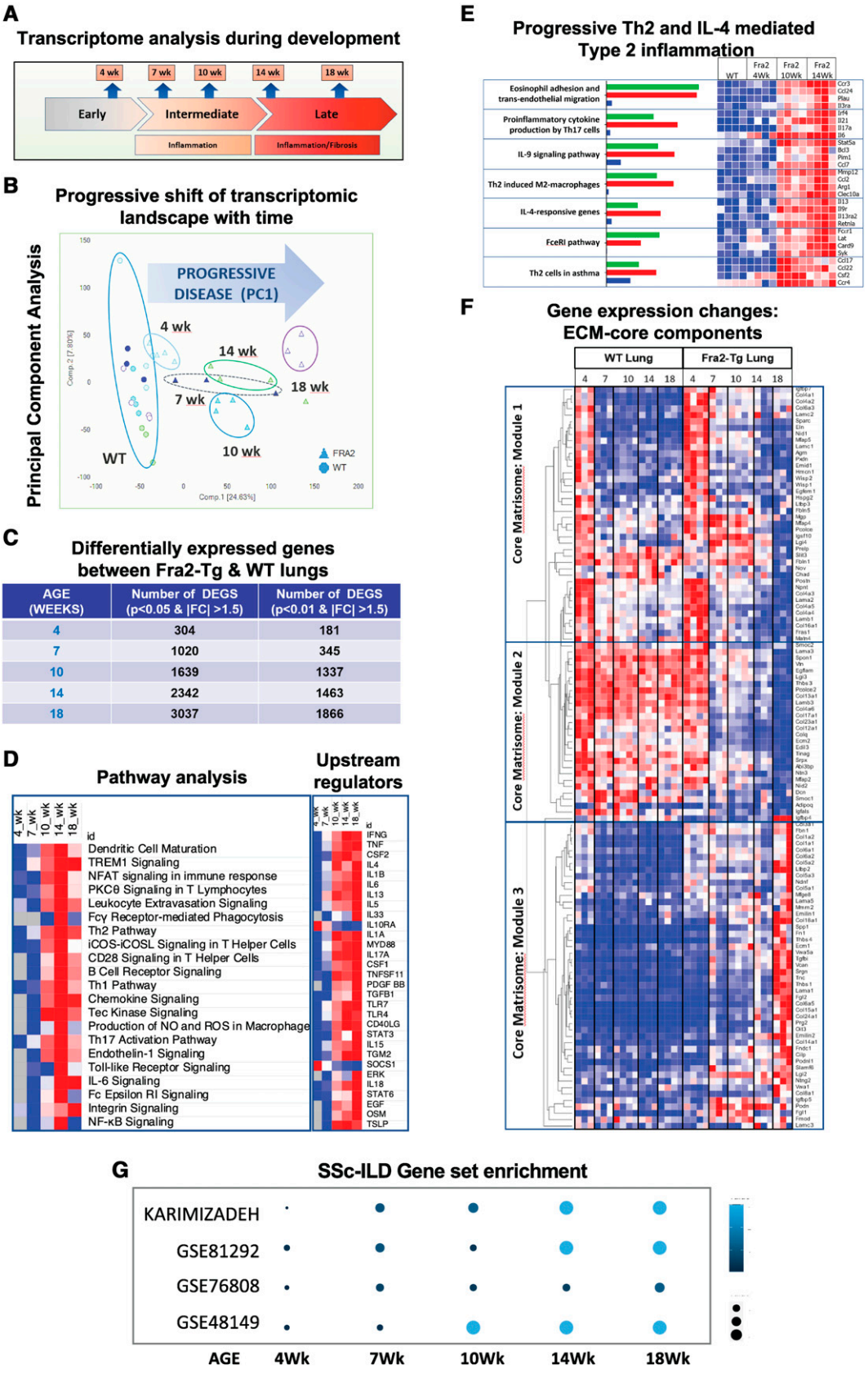

Figure 3. Temporal gene expression analysis identifies different stages of inflammation and tissue remodeling. (*A*) Experimental design showing the time-series snapshots of the lung transcriptome comparing FRA2-Tg lungs with littermate controls. (*B*) Principal component analysis of the

accumulation were apparent. In contrast, a loss of NK cell signature was observed early in FRA2-Tg lungs at 4 weeks of age, and this persisted up to 18 weeks. Although type 2 inflammation has previously been reported in the lungs of FRA2-Tg animals (12), we captured its progressive nature to deconvolve the sequence of events during the progression of FRA2-driven inflammation. Systemic autoimmunity in FRA2-Tg animals has been attributed to reduction in T regulatory cell (Treg) development (13), and, consistent with this, on the basis of upstream regulator analysis using IPA, a progressive decrease of FOXP3-mediated gene expression changes is observed (data not shown).

We next sought to analyze the pathways driving the fibrotic events through the transcriptional changes in profibrotic genes in these lungs. Using the core matrisome signature from the Matrisome Project (33) (http://matrisomeproject.mit.edu), gene expression changes of the core matrisome revealed three distinct gene modules (Figure 3F). Module 1 contained genes that were expressed in steady state at weaning (4 wk) and downregulated after lung development is complete. Although many of these genes follow a similar pattern in FRA2-Tg lungs (e.g., *Eln*, *Sparc*, and *Mfap5*), some genes in Module 1 show a distinct pattern in FRA2-Tg lungs (e.g., *Postn*, *Col4a3*, and *Col4a4*). Module 2 contained genes that stayed unchanged after lung development in steady state, but in FRA2-Tg lungs, these genes are shut down at the end stage of fibrosis (e.g., *Thbs3*, *Col17a1*, *Pcolce2*, and *Col12a1*). Module 3 contained genes that are not expressed in WT lungs but were highly upregulated in FRA2-Tg lungs (e.g., *Spp1*, *Fn1*, *Tnc*, *Thbs1*, *Col1a1*, *Col3a1*, and *Fbln1*). Module 3 likely represents the pathogenic signature of lung fibrosis in the FRA2-Tg lungs and contained genes and/or proteins that are elevated in human lung diseases such as IPF and SSc-ILD (34–37). Conversely, Module 1 is mostly composed of genes involved in establishing lung architecture: *Eln*, type IV collagens (*Col4a1*, *Col4a2*), *Sparc*, *Agrn*, and others that are generally expressed in the early phase of lung development and are downregulated by the time the lung is fully developed. A similar pattern of response was observed in FRA2-Tg lungs, although some genes do not reach the baseline seen in WT lungs, possibly because of the underlying inflammatory milieu (38, 39).

We next used gene set enrichment analysis (GSEA) on the DEGs from this study with signatures generated from lungs of patients with SSc-ILD (datasets GSE81292, GSE76808, GSE48149, and the compiled gene set generated from analysis done by Karimizadeh and colleagues [20]). Significant enrichment of the identified signatures developing with age in the FRA2-Tg mice with these disease-generated gene sets was observed by 14 weeks of age (Figure 3G).

Characterizing Immune Infiltrates Using Single-Cell RNA-Seq and Immune Profiling

Although the deconvolution of abundant cell types using gene signatures implicated roles for several cell types, we next used single-cell RNA-seq to better define specific immune cell changes. $CD45^+$ cells were isolated from digested lungs of WT and FRA2-Tg animals at 10 weeks of age using FACS sorting, and single-cell RNA-seq was performed on these cells. A total of 4,220 cells were analyzed in WT lungs, and 4,841 cells were analyzed from the FRA2-Tg lungs (Figure 4A). The immune cells from lungs were segregated into 10 distinct clusters, with 4 of the 10 clusters observed only in the FRA2-Tg lungs (Figure 4A and Figure E9A). As expected, most of the clusters showed elevated expression of FRA2 transcription factor in cells from FRA2-Tg animals (Figure 4A, inset). Manual analysis of cell-representative markers (Figure 4B) identified Clusters 1, 2, 3, and 4 as $CD3^+$ T cells, Cluster 5 as $NCR1^+$ NK cells, Clusters 6 and 7 as $CD20^+$ B cells, Cluster 8 as a mix of myeloid and granulocyte cell compartments ($CST3^+$). Clusters 9 and 10 were not classified on the basis of traditional cell type marker analysis.

To characterize the difference in each cell type, DEG analysis was performed for each cluster using the user-interactive cluster selection on the SPRING portal. Within the CD3-expressing T cell cluster, the comparison between $CD4^+$ T cells in Cluster 1 between the FRA2-Tg and WT genotypes showed marginal differences, with upregulation of genes associated with protein translation *Eef1b2*, *Tpt1*, and *Eef1a1* (Figures 4C and E9A). However, the cluster of $CD3^+CD4^+$ cells exclusively present in FRA2-Tg lungs (Cluster 4) showed an activated phenotype with upregulation of *Il2ra*, *Cd44*, *Lag3*, and *Lgals1* and *Lgals3*. The cells showed a Th2-skewed phenotype with increased expression of cytokine genes *Il4*, *Il5*, *Il13*, and *Areg* as well as the Th2 master regulator *Gata3* (Figures 4D and E10A). The CD4 population also showed enrichment of Th17 genes such as *Rorc* and *Il17a* (Figure E10B). The $CD4^+$ cells from FRA2-Tg lungs consistently showed reduced expression of *Il7r*, *Ccr7*, and *Lef1* consistent with an activated phenotype (Figures 4C and 4D). $CD8^+$ T cells from FRA2-Tg lungs also showed a shift with the appearance of a new subcluster (3) with elevated transcript levels of *Ctla2a*, *Ctla2b*, *Gzmm*, and *Ccl5*, among others, potentially representing an activated $CD8^+$ T cell phenotype (Figure 4E).

A marked shift in the transcriptional landscape of $CD20^+$ B cells was observed, with highly elevated levels of *S100a6*, *Vim*, *Cd44*, and *Mzb1* showing features of transformed B cells (Figure 4F). Consistent with the distinct B cell transcriptional landscape observed, we observed elevated anti-SLC-70 and anti-JO-1 autoantibodies in ~50% and ~23% of 16-week-old FRA2-tg animals, respectively (Figures E11A and

Figure 3. (*Continued*). transcriptome of lungs from FRA2-Tg and WT animals at different ages shows a progressive shift of the FRA2-Tg lung transcriptome to the right. FRA2-Tg lungs are shown as triangles, and WT littermates are shown as circles. (*C*) Table enumerating the number of differentially expressed genes (DEGs) that match the statistical criteria mentioned in the table headers, showing a modest difference at 4 weeks of age and an increasing shift of the whole transcriptome with an increasing number of DEGs. (*D*) Canonical pathway analysis and upstream regulator analysis of DEGs at different stages using the Ingenuity Pathway Analysis tool. Red cells depict increased *z*-scores and identify enhanced state of the specific pathway or upstream regulator. (*E*) Selected genes highlighting the temporal activation of pathways related to type 2 inflammation (blue bars = 4 wk; red bars = 10 wk; green bars = 14 wk). (*F*) Gene expression changes showing the state of matrisome proteins and tissue remodeling over 18 weeks of progressing lung disease. On the basis of their patterns of expression, these genes are divided into three gene modules. (*G*) Enrichment of gene sets derived from lung samples of patients with systemic sclerosis and interstitial lung disease (SSc-ILD) using gene set enrichment analysis. Color gradient shows the spectrum of enrichment scores, and the size of the bubble depicts the reverse log of the *P* value. ECM = extracellular matrix.

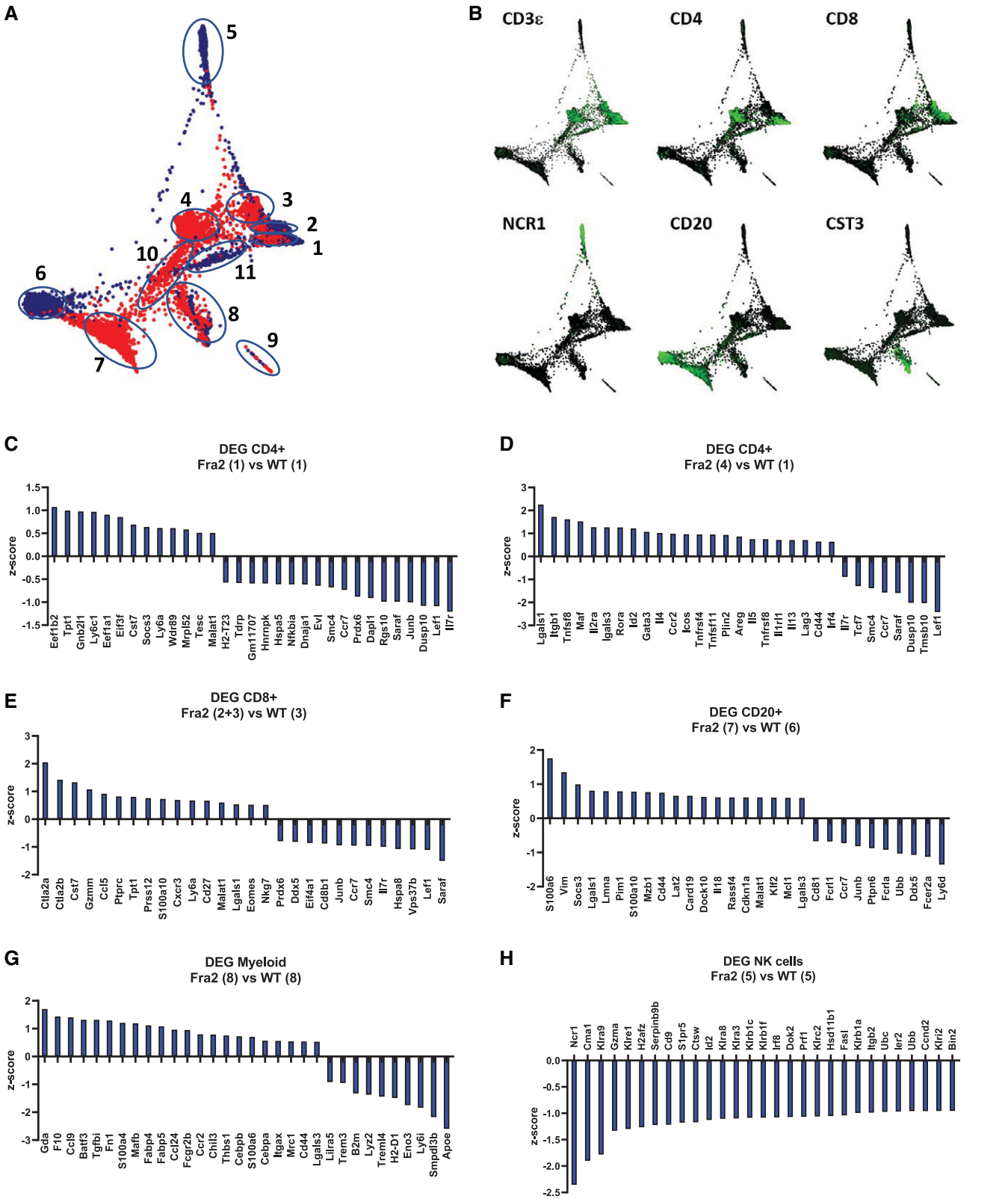

Figure 4. Immunophenotyping using single-cell RNA sequencing reveals a robust type 2 inflammatory response driven by $CD4^+$ T-helper type 2 cells. (*A*) single cell data analysis (SPRING) database single-cell RNA-sequencing plot of lungs from 10-week-old WT and FRA2-Tg animals shows altered cell states in FRA2-Tg animals. Clusters 1–11, highlighted, show different cell populations within the $CD45^+$ compartment. (*B*) SPRING database feature plots showing the distribution of *Cd3ε*$^+$, *Cd4*$^+$, and *Cd8*$^+$ T cells, *Cd20*$^+$ B cells, *Ncr1*$^+$ natural killer (NK) cells, and

E11B). This is consistent with clinical autoimmune disease, where elevated autoantibodies against SLC-70 and JO-1 distinguish SSc and antisynthetase syndrome, respectively, from healthy controls and correlating ILD and fibrosis (40, 41).

A comparison of the clusters with myeloid populations between the FRA2-Tg and WT genotypes revealed a profibrotic M2-like phenotype with elevated transcript levels of *Tgfbi*, *Fn1*, *Fabp4*, *Cebpa*, *S100a4*, *S100a6*, and *Mrc1* (Figures 4G and E10C). A drastic reduction in NK cell frequency was observed in the FRA2-Tg lungs, with the near-complete abrogation of this population. The rare NK cells observed in FRA2-Tg lungs also showed a distinct transcriptional profile with reduced levels of *Ncr1*, *Gzma*, and other markers characteristic of NK cells. This reduced NK cell frequency in FRA2-Tg lungs with robust type 2 inflammation is consistent with a recent finding showing the association of enhanced type 2 inflammation with NK cell paucity (42). These data from the single-cell RNA-seq analysis show a robust Th2 phenotype with an abundance of the M2-like macrophage phenotype in the FRA2-Tg lungs with a "rogue" B cell phenotype reminiscent of transformed B cells. These data are consistent with the observations from the bulk RNA-seq data reported in the previous section (Figure 4F).

Flow cytometric analysis was performed to expand on these initial findings of differential cellular complexity of the lung immune infiltrate, with a focus on the early stage (4 wk), intermediate stage (10 wk), and late stage (18 wk) of progressive lung disease. Consistent with the bulk RNA-seq data in Figure 3, which showed a noninflammatory state across all cell types, the T cells of the activated $CD44^+$ phenotype were comparable between the FRA2-Tg and WT lungs early but progressively increased during the intermediate and late stages of the lung pathology (Figure 5A). This was concurrent with elevated frequencies of Th2, as determined by the presence of GATA3 (Figures 5B and E12E) and RAR-related orphan receptor γT–expressing Th17 cells (Figures E12B and E12D), whereas T-bet–expressing Th1 phenotype cells were unaffected (Figures E12A and E12C).

In addition to these alterations in T cells, significant increases in the frequency of DCs, eosinophils, and $CD11b^+CD64^-$ macrophages were observed, whereas NK cells showed dramatic reductions in FRA2-Tg animals (Figures 5D and 5F–5H). The increase in DC numbers was most significant at 4 weeks of age, and the differences became less apparent with time. This is consistent with the gene signatures described in Figure 3, where the signatures of these respective cell types were markedly increased. The loss of NK cells was drastic across all ages, with a significant reduction in the proportion and number of NK cells. In agreement with a recent study (43), robust expansion of M2 macrophages ($CD206^+$) was also observed early, persisted to 18 weeks of age, and was reflected in the transcriptional landscape of the FRA2-Tg lung (Figures E13A and E13B). Eosinophil frequencies are elevated in FRA2-Tg lungs at 4 weeks of age, and the differences become more apparent by 10 and 14 weeks (Figures 5F–5H). This is consistent with the observation of ECP in the lungs and elevated eosinophils observed in BAL, as described previously, and aligned with elevated *Cxcl12* and *Il5* levels in the FRA2-Tg lung. Besides their increased frequencies, the eosinophils appear to switch from a regulatory state, as described in the murine lung (44), to an inflammatory state with increased expression of *Cd101*, *Retnla*, and *Il1rn* (Figure E14). However, gene expression analysis of sorted eosinophils from 16-week-old WT and FRA2-Tg animals revealed a mixed phenotype, with FRA2 eosinophils showing an IL-4–, IL-1RN–, and IL-13–dominated response with high expression of *Col6a5*, *Arg1*, *Il1rn*, and *Chil3* and reduced expression of *Il12b*, *Ctnnd2*, *Cd74*, and *Cst3* (Figure 5I). The differential phenotype seems to be a result of eosinophil activation downstream of *Il1rn*, *Il4*, and *Il13*, as demonstrated by upstream regulator analysis of the DEGs (Figure 5J).

Targeting Type 2 Inflammation Using IL-4/IL-13 Antibody Reverses the Lung Pathology

Given that the FRA2-Tg mice present predominantly with type 2 inflammation, we next examined the effects of therapeutically targeting IL-4 and IL-13 using a neutralizing bispecific antibody against IL-4 and IL-13. Initial pharmacokinetic studies were performed, and once-weekly dosing at 10 mg/kg was identified as optimal on the basis of an *ex vivo* pSTAT6 assay (data not shown). The antibody treatment of the FRA2-Tg animals and controls was performed at the peak of the inflammatory response between 10 and 14 weeks of age, and the impact on the global lung transcriptome and lung pathology was assessed.

After the antibody treatment, a significant reversal of the lung pathology in the FRA2-Tg animals was observed, with reduction in immune cell infiltrates and tissue remodeling (Figures 6A and 6B) and lung weights (Figure 6C). In addition, FRA2-Tg animals showed decreased lung function compared with littermate control animals, which was partially recovered after treatment with a bispecific antibody against IL-4 and IL-13, also reflected in reduced lung weights from antibody-treated FRA2-Tg animals (Figures E15A and E15B). As mentioned earlier, FRA2-Tg mice present with significantly increased eosinophil and M2 macrophage density, and both of these are significantly reduced after antibody treatment (Figures 6D, 6E, and E15C). Consistent with the reduction in immune infiltrates, activated total $CD4^+CD44^{hi}$ T cells and $CD4^+CD44^{hi}$ $GATA3^+$ T cells, as well as $CD206^+$ M2 macrophages, were also reduced (Figures 6F and 6G).

The transcriptome of the groups treated with isotype control antibody was distinct between the FRA2-Tg and control animals, as shown in Figure 3, and this picture was more or less unchanged at the global scale in animals treated with an αIL-4/IL-13 antibody, except for a subset of genes whose patterns reversed partially or completely to the WT levels (Figure 7A). Although histological analysis of lung tissue revealed abrogation of lung pathology to a large extent, a total of 1,569 genes showed a shift in gene expression (log fold change, 1.3; false discovery rate, <0.05) after αIL-4/IL-13 antibody treatment, which is only a fraction of the DEGs between WT and FRA2-Tg

Figure 4. (*Continued*). *Cst3*$^+$ myeloid cells. (*C*) Top DEGs between *Cd4*$^+$ cells from FRA2-Tg and WT lungs within Cluster 1. (*D*) Top DEGs between *Cd4*$^+$ cells from FRA2-Tg (Cluster 4) and WT lungs (Cluster 1). (*E*) Top DEGs between *Cd8*$^+$ cells from FRA2-Tg (Clusters 2 and 3) and WT lungs (Cluster 2). (*F*) Top DEGs between *Cd20*$^+$ B cells from FRA2-Tg (Cluster 7) and WT lungs (Cluster 6). (*G*) Top DEGs between *Cst3*$^+$ myeloid cells from FRA2-Tg and WT lungs within Cluster 8. (*H*) Top DEGs between *Ncr1*$^+$ NK cells from FRA2-Tg and WT lungs within Cluster 5.

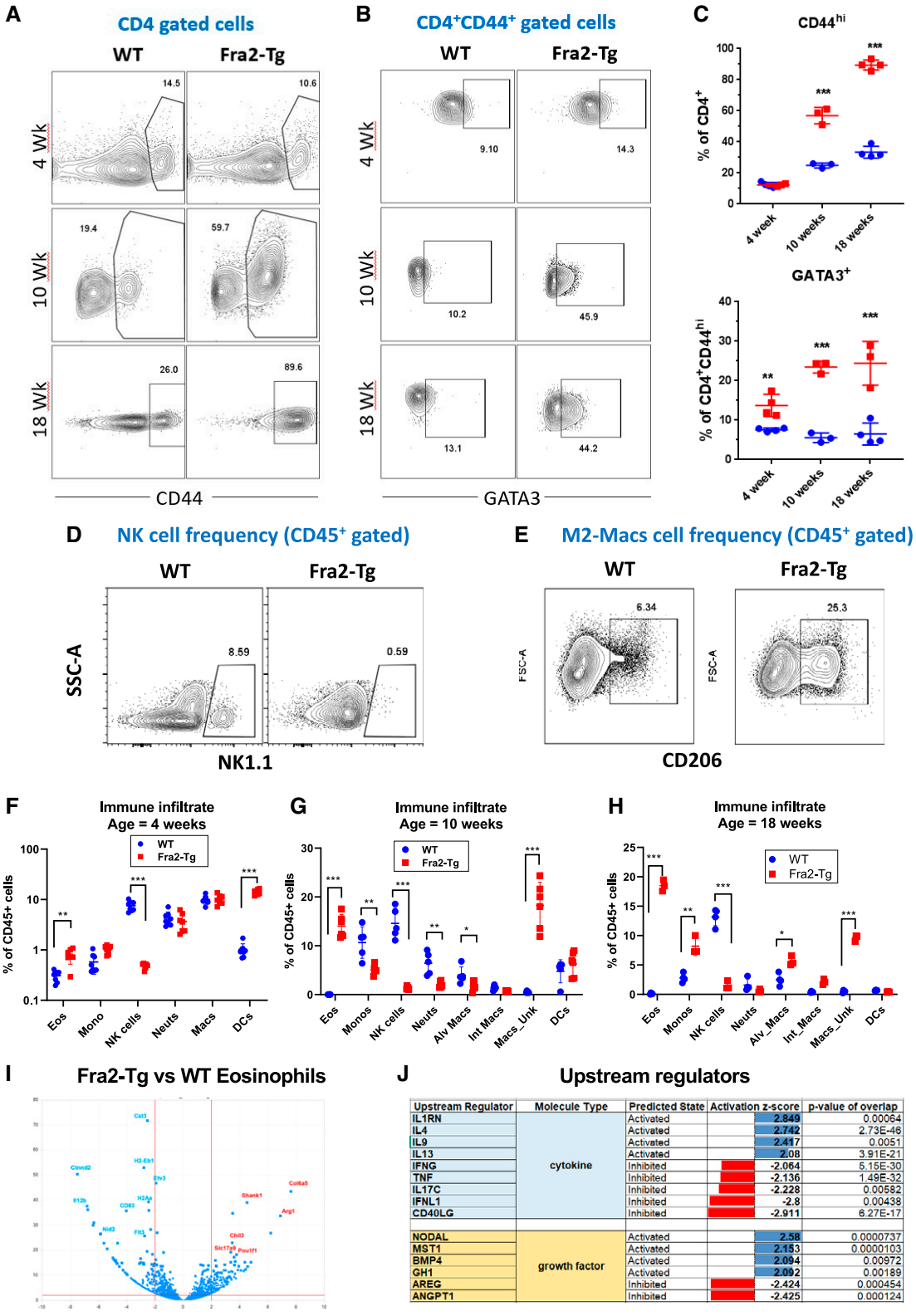

Upstream Regulator	Molecule Type	Predicted State	Activation z-score	p-value of overlap
IL1RN	cytokine	Activated	2.849	0.00064
IL4		Activated	2.742	2.73E-46
IL9		Activated	2.417	0.0051
IL13		Activated	2.08	3.91E-21
IFNG		Inhibited	-2.064	5.15E-30
TNF		Inhibited	-2.136	1.49E-32
IL17C		Inhibited	-2.228	0.00582
IFNL1		Inhibited	-2.8	0.00438
CD40LG		Inhibited	-2.911	6.27E-17
NODAL	growth factor	Activated	2.58	0.0000737
MST1		Activated	2.153	0.0000103
BMP4		Activated	2.094	0.00972
GH1		Activated	2.092	0.00189
AREG		Inhibited	-2.424	0.000454
ANGPT1		Inhibited	-2.425	0.000124

Figure 5. Immunophenotypic characterization of FRA2-Tg lungs using flow cytometry reveals a robust type 2 and type 17 inflammatory response. (*A*) Representative flow cytometry plots of $CD4^+$ gated cells from FRA2-Tg and WT littermate control mouse lungs showing a proportion of activated $CD44^{high}$ cells at 4 weeks, 10 weeks, and 18 weeks of age. (*B*) Representative flow cytometry plots of $CD4^+CD44^{high}$ gated cells from FRA2-Tg and WT littermate control mouse lungs showing the proportion of $GATA3^+$ T-helper type 2 cells at 4 weeks, 10 weeks,

lungs. The major pathways impacted were type 2 inflammation, the complement system, eukaryotic initiation factor 2 signaling, production of nitric oxide and reactive oxygen species by macrophages, leukocyte extravasation signaling, and oxidative phosphorylation (Figure 7B). Upstream regulator analysis using IPA revealed that pathways downstream of cytokines IL-4, TNF, IL-13, IL-5, IL-1β, CSF2, and IL-33, among others, are downregulated. In addition, there appears to be a shutdown of Toll-like receptor and CD40 signaling. Interestingly, there appears to be an increase in some pathways downstream of MEF2C, MYOCD, STAT5B, SOCS1, IL10RA, APOE, and INSIG1 in FRA2-Tg lungs after αIL-4/IL-13 antibody treatment (Figure 7C). Enrichment analysis of immune gene signatures from MSigDb revealed a major shift in pathways related to $CD4^+$ and $CD8^+$ T cell activation, macrophage polarization, and DC maturation (Table E2). Genes associated with tissue remodeling and fibrosis were also significantly impacted (Figure 7D), with a significant reduction in collagens such as *Col1a1*, *Col3a1*, and *Col6a1* as well as other ECM-related genes, including *Tgfbi*, *Fn1*, and *Vcan*. The impact of the antibody on fibrosis was further validated using the nanostring murine fibrosis panel by analyzing the 770 tumor- and fibrosis-related genes (Figures 7E and E16).

GSEA of the antibody-treated group using gene signatures derived from publicly available gene expression datasets from SSc-ILD revealed that many of these signatures are impacted after treatment of FRA2-Tg animals with αIL-4/IL-13 antibody (Figure 7F). These results imply that therapeutic targeting of IL-4/IL-13 biology tunes down the overall ongoing inflammation in FRA2-Tg lungs.

Discussion

The potential role of type 2 inflammation in establishing pathogenic fibrosis, such as that observed in SSc and chronic ILDs such as IPF, has been reported for many years but is based largely on data mostly from mouse models or associations observed in human studies. The availability of tissue-relevant transcriptomic data from fibrotic diseases such as IPF and SSC-ILD has made it possible to back-translate the findings from human datasets to insights into the potential mechanisms of the pathogenesis and altered immune and physiological states in these diseases and has strengthened the utility of animal models as a path to translate to human disease.

Here, we sought to characterize the events involved in key phases of fibrosis development and so took advantage of the robust spontaneous inflammation and fibrosis previously described by us and others (11, 14) that showed similarities in the lung pathology of patients with SSc-ILD (11, 14). The inflammation in the pulmonary compartment increased with age along with increased collagen deposition and decreased pulmonary function. This aggressive inflammation is likely explained at least partially by a recent finding showing that FRA2 attenuates the development of Tregs (13), which we also observed using pathway analysis for Treg signatures (data not shown). The role of FRA2 in driving fibrosis has also been attributed to the downregulation of LRP1 and activation of TGF-β signaling, resulting in ECM deposition, by enhancing the phagocytosis of fibroblasts (45, 46). In a recent report, a potential role FRA2 in driving SSc myofibroblast differentiation has been suggested using SCENIC (single-cell regulatory network inference and clustering), a computational method predicting transcriptional factor networks. The myofibroblast transcriptome indicates $SFRP2^{hi}$ fibroblast progenitors in SSc skin (47). However, these studies suggest independent mechanisms behind the inflammatory and fibrotic components of the model. Also, there has been a discrepancy in the model regarding the sufficiency of the lymphoid compartment in driving the pathogenesis in FRA2-Tg mice (11, 13). Given that the mice used in this study were rederived the same as in the study by Renoux and colleagues (13), our findings align with that study in terms of what appears to be a T cell– and B cell–driven phenomenon.

Using public data from lung biopsies of patients with SSc-ILD, we identified multiple type 2 inflammatory modulators, such as IL-4, IL-5, IL-13, and IL-33, as upstream regulators of genes differentially regulated in the lungs of patients with SSc-ILD (15, 16). We then investigated these type 2 pathways in the transcriptomic data from the lungs of the FRA2-Tg model at different stages of progressive pathology and identified different cellular and molecular mediators of inflammation and fibrosis. This study captures different phases of disease and can be a rich source of hypotheses related to pathomechanisms underlying lung fibrosis in SSc-ILD beyond what we present in this article. The transcriptional profile of lungs from 4-week-old mice showed a relatively smaller transcriptional shift, indicating that the effects mediated by the FRA2 transgene are in the early phase. However, robust transcriptional changes were apparent soon after, at 7 and 10 weeks of age, with maximum transcriptional shift peaking at the study endpoint of 18 weeks. Elevated expression of *Csf2* and *Cxcl12* early in lung inflammation could be viewed as a precursor to an ensuing fibrotic program. The receptors for these molecules, MCSFR and CXCR4, have been implicated in promoting and sustaining fibrosis. Macrophage colony-stimulating factor receptor–expressing monocyte-derived macrophages are found in fibrotic niches (48), $CXCR4^+$ cells are increased in lung tissues of patients with IPF (49), and inhibition of signaling from these receptors ameliorates fibrosis (50, 51). Some

Figure 5. (*Continued*). and 18 weeks of age. (*C*) Frequency of $CD4^+CD44^{high}$ and $CD4^+CD44^{high}GATA3^+$ cells in mouse lungs at 4 weeks, 10 weeks, and 18 weeks of age (error bars represent mean ± SE; $^{***}P < 0.001$ and $^{***}P < 0.0001$). (*D*) Representative $CD45^+$ gated cells from lungs of WT and FRA2-Tg animals showing the frequency of $NK1.1^+$ cells. (*E*) Representative $CD45^+$ gated cells from lungs of WT and FRA2-Tg animals showing the frequency of $CD206^+$ M2-like macrophages. (*F*) Frequency of eosinophils, monocytes, NK cells, neutrophils, macrophages, and dendritic cells depicted as percentages among $CD45^+$ gated cells from lungs of WT and FRA2-Tg animals at 4 weeks of age. (*G*) Frequency of eosinophils, monocytes, NK cells, neutrophils, macrophages, and dendritic cells depicted as percentages among $CD45^+$ gated cells from lungs of WT and FRA2-Tg animals at 10 weeks of age. (*H*) Frequency of eosinophils, monocytes, NK cells, neutrophils, macrophages (alveolar, interstitial, and unconventional), and dendritic cells depicted as percentages among $CD45^+$ gated cells from lungs of WT and FRA2-Tg animals at 18 weeks of age. (*I*) Volcano plot showing DEGs between eosinophils isolated from FRA2-Tg and WT littermate controls at 16 weeks of age. The *x*-axis shows the fold change, and the *y*-axis shows the *P* value. (*J*) Upstream regulator analysis from Ingenuity Pathway Analysis showing the major cytokines and growth factors that drive the inflammatory eosinophil phenotype in FRA2-Tg mouse–derived eosinophils. $^*P < 0.05$, $^{**}P < 0.01$, $^{***}P < 0.001$, and $^{****}P < 0.0001$.

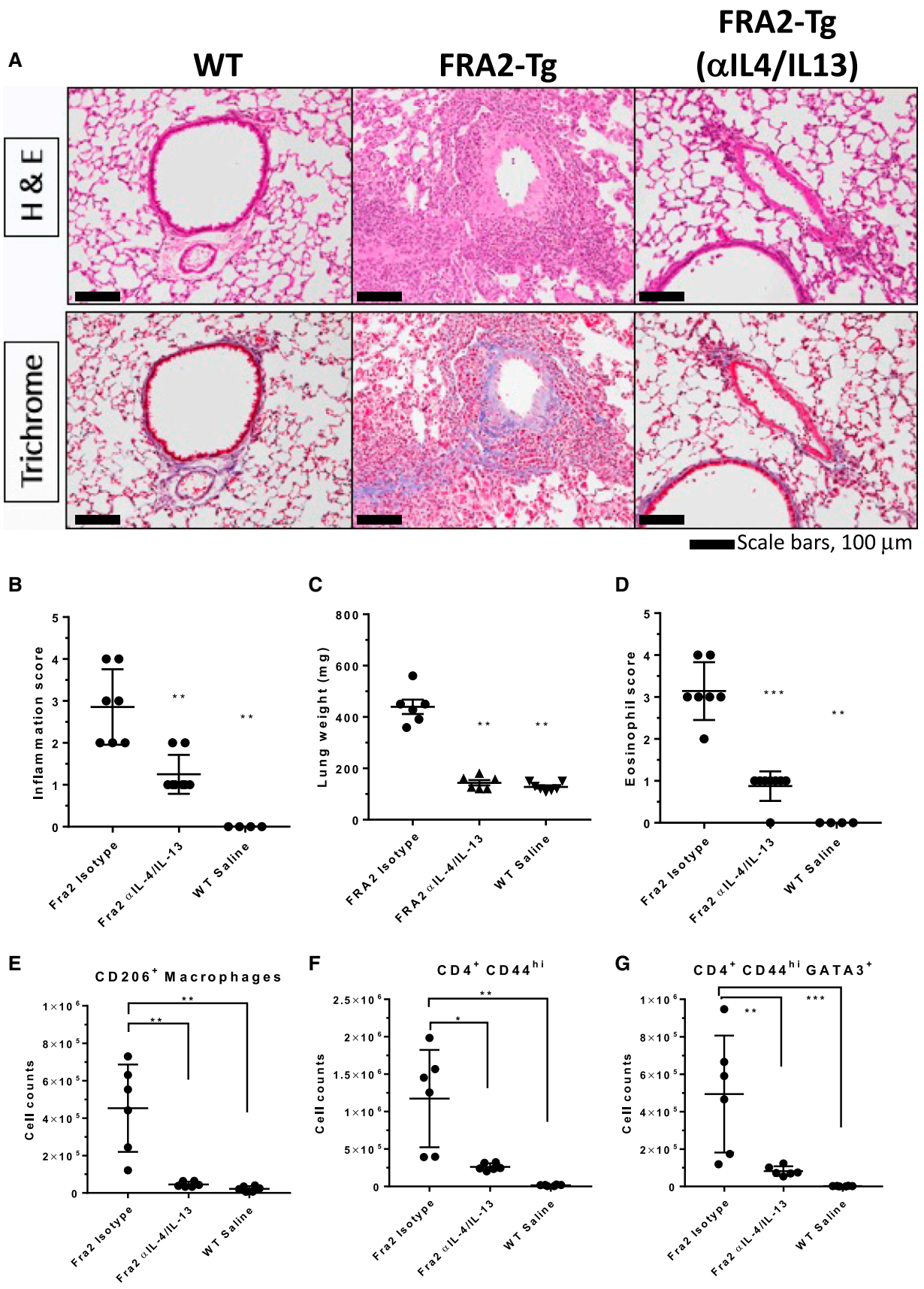

Figure 6. Treating FRA2-Tg mice with the bispecific antibody blocking IL-4 and IL-13 shows reversal of lung inflammation and tissue remodeling. (*A*) Representative images of hematoxylin and eosin (H&E)– and Masson trichrome–stained lungs from vehicle-treated or anti-IL-4/IL-13 antibody–treated FRA2-Tg mice (middle and right panels) and the vehicle-treated WT littermate controls (left panels), showing the reversal of

of the most prominent pathways underlying lung fibrosis in FRA2-Tg animals have been attributed to Th2 expansion and M2 macrophage infiltration (12, 43, 52), and our data clearly show a progressive accumulation of these cells, along with eosinophils, neutrophils, and DCs, starting early at 7 weeks, as also apparent at cell abundance level and a drastic reduction in NK cell frequencies. Murine NK cell deficiency has recently been associated with enhanced type 2 inflammation (52). AP-1 transcription factors, including FRA2, have been reported to play important roles in regulating NK function, cytotoxicity, and surface receptor expression (53). FRA2-Tg animals have also been associated with reduced NK cell frequencies as a result of a significant reduction in Nfil3, which is essential for the transition of common lymphoid cells to NK-committed precursor cells and an AP-1 binding site in the promoter of this gene (54). In addition, TGF-β–driven AP1 induction mediates starvation-induced NK cell death, reduced expression of antiapoptotic proteins such as Bcl2, and reduced Akt phosphorylation after NKG2D activation (55). The impact of the FRA2 transgene on NK cell development is likely cell intrinsic and could argue for a regulatory role of tissue-resident NK cells in inflammation.

A deep dive into the modulation of matrix-associated proteins shows a subset of tissue remodeling genes (Module 3) that are progressively elevated and peak at 18 weeks of age, which also reflects the most aggressive lung fibrosis and highly compromised lung function. This progressive trend is also clear when gene modules derived from human SSc-ILD lungs (and skin) are investigated, with maximum enrichment of these modules apparent at the fibrotic stage. Many of these findings were further elaborated at the cell type level with a clear expansion of Th2 cells, with expansion of *Il4*-, *Il5*-, *Il13*-, and *Il17*-expressing $CD4^+$ T cells. Within the mix of cells within the myeloid cluster, interestingly, there was a significant enrichment of genes from M2 macrophages as well as some of profibrotic genes, such as *Tgfbi* and *Fn1*. These data lend further granularity to the transcriptional data at the bulk level. Elevated expression of S100a4 and *S100a6* in FRA2 lungs is consistent with findings from human patients with IPF (56) and SSc-ILD (57), in whom *S100a6* has been reported as a potential biomarker of lung fibrosis. Increased expression of *Fabp4* and *Cebpa* in lungs from FRA2 mice, however, is contrary to observations in human fibrosed lungs because expression of FABP4 in proliferating macrophage populations decreases in IPF lungs (34). Similarly, CEBPA expression is decreased in IPF lung–derived fibroblasts (58), highlighting the discrepancy between human disease and murine models that do not capture the complexity of human biology in its entirety. *Cebpa* and *Cebpb* are experimentally known targets of FRA2, based on the STRING database (data not shown) (59), and could be upregulated in cells with nonphysiological FRA2 expression. *Fabp4* gene expression may be modulated by similar differential mechanisms that need to be explored further.

Unlike what was previously reported by Maurer and colleagues (60), we observed autoantibodies in 16-week-old FRA2-Tg mice but not younger FRA2-Tg mice or any of the WT mice. More specifically, autoantibodies against SLC-70 were observed in ∼50% of mice and JO-1 in ∼23% of mice, with 100% overlap between mice showing JO-1 and SLC-70 autoantibodies. Given that SLC-70 and JO-1 autoantibodies are highly specific to SSc and antisynthetase syndrome, respectively, and correlate with pulmonary involvement in these diseases (61, 62), these results suggest that a subset of these FRA2-Tg mice develop an SSc-like and antisynthetase syndrome–like disease. However, it is currently unclear whether the presence of autoantibodies confers a worse outcome in these mice. Future work is warranted to better characterize the consequences of having autoantibodies in FRA2-Tg mice.

Recent clinical studies have shown that targeting IL-13 alone with tralokinumab or lebrikizumab has no benefit in blocking the progression of IPF (63, 64). Similarly, SAR156597, targeting IL-4 and IL-13, showed no efficacy in attenuating the progression of IPF (65). However, SAR156597 demonstrated significant effects on changes in the skin when administered to patients with diffused cutaneous scleroderma in a phase II clinical trial demonstrating the benefits of concomitant targeting of IL-4 and IL-13 to treat fibrosis (10). The discordant outcomes from the two fibrotic conditions after targeting the two type 2 cytokines suggest a role for these cytokines in promoting fibrosis that is accompanied by inflammation in conditions such as SSc, differentiating it from IPF, in which an active inflammatory component may not be critical in driving disease progression (66, 67). To gain further understanding and to establish a role of type 2 inflammation in driving SSc-ILD-like lung pathology in FRA2-Tg animals, we used the αIL-4/IL-13 antibody, a bispecific IL-4– and IL-13–neutralizing antibody intervention, at Week 10, a stage when inflammation is at its peak and fibrosis has been initiated. The bispecific IL-4/IL-13 antibody was efficacious in suppressing the inflammation, led to a reduction in established M2 macrophage population, and significantly decreased collagen deposition, suggesting that targeting IL-4 and IL-13 has the potential to effectively attenuate type 2 inflammation and block the progression of fibrosis. Using blockade of IL-4 and IL-13 and performing transcriptomic analysis of treated lungs, we identified gene modules driving type 2 inflammation and fibrosis in these lungs and showed significant blunting of pathways associated with SSc-ILD. Most of the DEGs in the lungs from FRA2-Tg and WT animals were not impacted by antibody treatment, highlighting the extent of aggressive developmental changes that are driven by the FRA2 transgene and the selective effects of the αIL-4/IL-13 antibody treatment in ameliorating inflammation-associated fibrosis. It is important to note that when nintedanib was used in this model, there was a significant reduction in M2 macrophages, suggesting that nintedanib may also modulate this biology (68). On the

Figure 6. (*Continued*). constricted alveoli and vasculature. Scale bars, 100 μm. (*B*) Scatter dot plots of total inflammation score as assigned by the expert pathologist. (*C*) Scatter dot plots of total lung weights from FRA2-Tg and WT animals at the time of euthanasia. (*D*) Scatter dot plots of eosinophil density score as assigned by the expert pathologist. (*E*) Absolute cell counts of $CD206^+$ macrophages after blockade of IL-4 and IL-13. (*F*) Absolute cell counts of $CD4^+CD44^{high}$ T cells. (*G*) Absolute cell counts of $CD4^+CD44^{high}GATA3^+$ T cells. Plots represent mean ± SD, and significant differences determined using the *t* test are marked with asterisks (**$P < 0.01$ and ***$P < 0.001$).

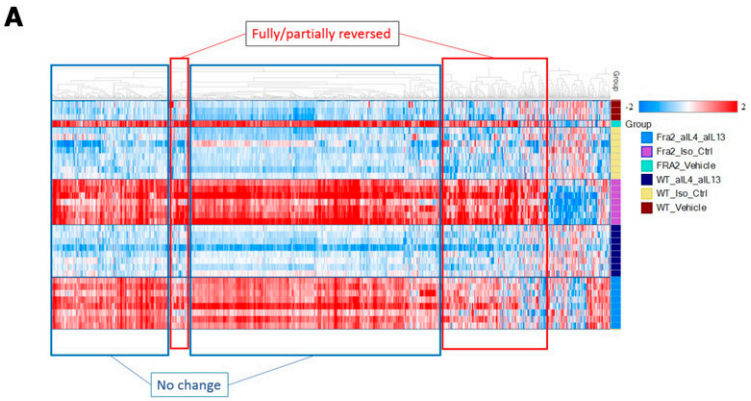

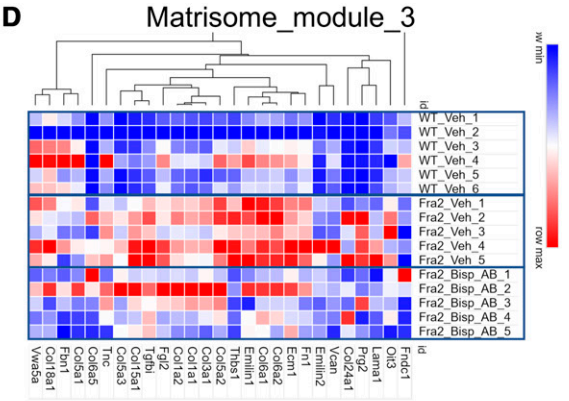

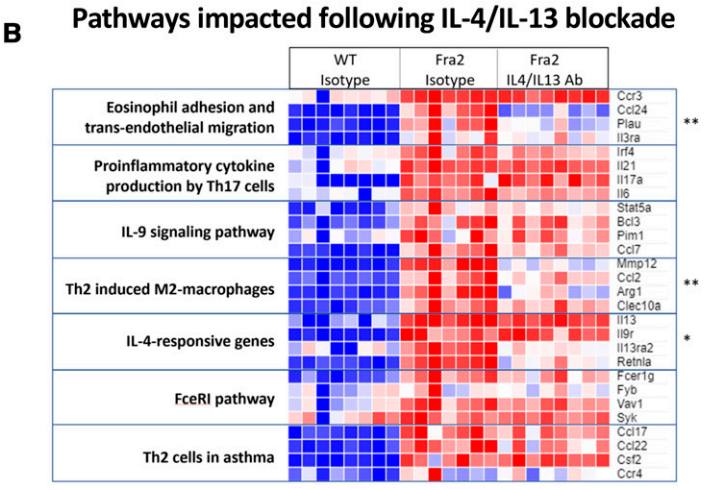

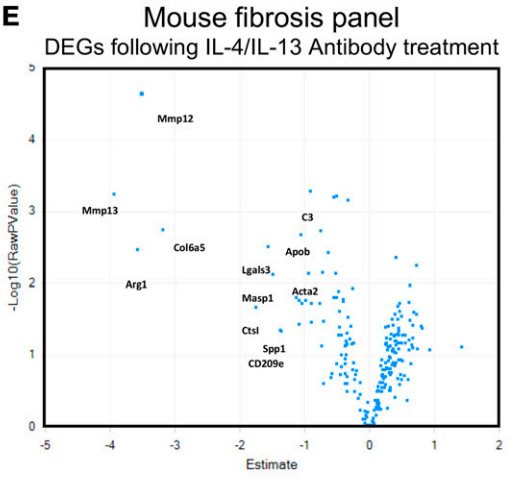

C
Upstream regulator analysis

Upstream Re	Molecule Type	Activation z-score	p-value (overlap)
CSF2	cytokine	-4.654	1.17E-11
IL4		-4.45	3.01E-29
TNF		-4.181	3.44E-43
IL1B		-4.09	3.45E-29
IL2		-4.083	6.67E-17
IL5		-4.056	1.11E-11
OSM		-3.863	1.85E-11
IL6		-3.723	3.52E-24
IL15		-3.566	5.15E-12
IFNG		-3.525	6.86E-30
IL21		-3.401	0.000000164
CD40LG		-3.357	1.21E-13
IL13		-3.234	7.23E-30
IL17A		-2.587	3.37E-13
IL33		-2.584	1.79E-08
EGF	growth factor	-2.665	3.94E-24
AREG		-2.102	0.000181
CD44	other	-3.559	7.56E-11
MYD88		-2.473	6.47E-15
MYOC		-2.433	0.000564
SOCS1		2.735	0.00000321
TSC2		2.797	1.86E-10
INSIG1		3.081	5.39E-10

Upstream Re	Molecule Type	Activation z-score	p-value (overlap)
SPI1	TF	-3.249	1.29E-11
STAT6		-2.813	9.34E-16
MITF		-2.541	6.72E-08
CEBPA		-2.35	2.56E-16
STAT5B		2.283	1.93E-09
SRF		3.089	1.46E-17
MYOCD		3.574	0.0000048
MEF2C		4.125	3.05E-19
Ige	complex	-4.051	3.32E-16
CD3		-3.609	4.92E-10
PDGF BB		-2.841	8.7E-15
Ap1		-2.256	6.78E-11
TLR4	receptor	-3.34	7.16E-10
TLR7		-3.217	0.0000923
TLR9		-3.049	0.000000367
CD40		-2.736	2.55E-08
TLR3		-2.595	0.000000314
IGF1R		2.393	0.000607
IL10RA		3.357	1.04E-12
BCL2	transporter	-2.292	0.000000694
BAX		-2.191	0.00131
APOE		2.733	5.63E-12

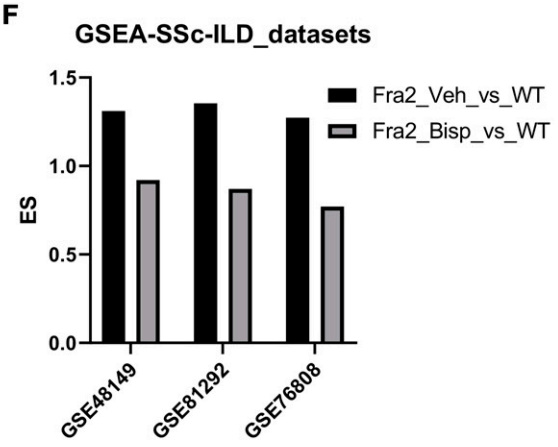

Figure 7. Gene expression analysis identifies pathogenic type 2 responses that are blocked after blockade of IL-4 and IL-13. (*A*) Hierarchical clustering of most variable genes across conditions shows a partial reversal of a subset of genes. Panel legend identifies groups; genes reduced in expression partially or fully after antibody treatment are enclosed in red boxes. (*B*) Pathway analysis of the transcriptome of lungs from FRA2-Tg and WT animals focusing on type 2 inflammatory pathways shows a partial reversal after blockade of IL-4 and IL-13. (*C*) Table enumerating the number of DEGs that match the statistical criteria mentioned in the table headers, showing a modest difference at 4 weeks of age and an increasing shift of the whole transcriptome with an increasing number of DEGs. (*D*) Hierarchical clustering of genes in matrisome module 3 showing reversal of most tissue remodeling–associated genes after antibody treatment. (*E*) Volcano plot showing the most differentially expressed genes in the nanostring analysis performed on RNA isolated from animals in the antibody-treated or untreated groups. (*F*) GSEA of gene sets derived from lung datasets from patients with SSc-ILD shows normalized enrichment scores in data from animals treated with the vehicle or the bispecific IL-4 and IL-13 antibody. GSEA = gene set enrichment analysis.

basis of our knowledge of shared pathways associated with the progression of fibrosis, our findings on the beneficial effects of inhibiting IL-4 and IL-13 in the attenuation of fibrosis in the lungs of FRA-2 mice support its value in the treatment of ILD associated with SSc. ■

Author disclosures are available with the text of this article at www.atsjournals.org.

Acknowledgment: The authors acknowledge Richa Hanamsagar and Mathew Chamberlain for single-cell support; Megan Pike, Jennifer Johnson, Keith Graver, and Riyun Huang for vivarium support; and Cynthia Shapiro and the histology team for histotechnological support.

References

1. Wick G, Grundtman C, Mayerl C, Wimpissinger TF, Feichtinger J, Zelger B, *et al.* The immunology of fibrosis. *Annu Rev Immunol* 2013;31: 107–135.
2. Wynn TA. Cellular and molecular mechanisms of fibrosis. *J Pathol* 2008; 214:199–210.
3. Wynn TA, Ramalingam TR. Mechanisms of fibrosis: therapeutic translation for fibrotic disease. *Nat Med* 2012;18:1028–1040.
4. Bradding P, Pejler G. The controversial role of mast cells in fibrosis. *Immunol Rev* 2018;282:198–231.
5. Reyfman PA, Walter JM, Joshi N, Anekalla KR, McQuattie-Pimentel AC, Chiu S, *et al.* Single-cell transcriptomic analysis of human lung provides insights into the pathobiology of pulmonary fibrosis. *Am J Respir Crit Care Med* 2019;199:1517–1536.
6. Pattanaik D, Brown M, Postlethwaite BC, Postlethwaite AE. Pathogenesis of systemic sclerosis. *Front Immunol* 2015;6:272.
7. Allanore Y, Simms R, Distler O, Trojanowska M, Pope J, Denton CP, *et al.* Systemic sclerosis. *Nat Rev Dis Primers* 2015;1:15002.
8. Gasparini G, Cozzani E, Parodi A. Interleukin-4 and interleukin-13 as possible therapeutic targets in systemic sclerosis. *Cytokine* 2020;125: 154799.
9. Huang XL, Wang YJ, Yan JW, Wan YN, Chen B, Li BZ, *et al.* Role of anti-inflammatory cytokines IL-4 and IL-13 in systemic sclerosis. *Inflamm Res* 2015;64:151–159.
10. Allanore Y, Wung P, Soubrane C, Esperet C, Marrache F, Bejuit R, *et al.*; Investigators. A randomised, double-blind, placebo-controlled, 24-week, phase II, proof-of-concept study of romilkimab (SAR156597) in early diffuse cutaneous systemic sclerosis. *Ann Rheum Dis* 2020;79: 1600–1607.
11. Eferl R, Hasselblatt P, Rath M, Popper H, Zenz R, Komnenovic V, *et al.* Development of pulmonary fibrosis through a pathway involving the transcription factor Fra-2/AP-1. *Proc Natl Acad Sci USA* 2008;105: 10525–10530.
12. Gungl A, Biasin V, Wilhelm J, Olschewski A, Kwapiszewska G, Marsh LM. Fra2 overexpression in mice leads to non-allergic asthma development in an IL-13 dependent manner. *Front Immunol* 2018;9: 2018.
13. Renoux F, Stellato M, Haftmann C, Vogetseder A, Huang R, Subramaniam A, *et al.* The AP1 transcription factor Fosl2 promotes systemic autoimmunity and inflammation by repressing Treg development. *Cell Rep* 2020;31:107826.
14. Elhai M, Avouac J, Hoffmann-Vold AM, Ruzehaji N, Amiar O, Ruiz B, *et al.* OX40L blockade protects against inflammation-driven fibrosis. *Proc Natl Acad Sci USA* 2016;113:E3901–E3910.
15. Barrett T, Wilhite SE, Ledoux P, Evangelista C, Kim IF, Tomashevsky M, *et al.* NCBI GEO: archive for functional genomics data sets—update. *Nucleic Acids Res* 2013;41:D991–D995.
16. Trapnell C, Pachter L, Salzberg SL. TopHat: discovering splice junctions with RNA-Seq. *Bioinformatics* 2009;25:1105–1111.
17. Trapnell C, Williams BA, Pertea G, Mortazavi A, Kwan G, van Baren MJ, *et al.* Transcript assembly and quantification by RNA-Seq reveals unannotated transcripts and isoform switching during cell differentiation. *Nat Biotechnol* 2010;28:511–515.
18. Weinreb C, Wolock S, Klein AM. SPRING: a kinetic interface for visualizing high dimensional single-cell expression data. *Bioinformatics* 2018;34:1246–1248.
19. Christmann RB, Sampaio-Barros P, Stifano G, Borges CL, de Carvalho CR, Kairalla R, *et al.* Association of interferon- and transforming growth factor β-regulated genes and macrophage activation with systemic sclerosis-related progressive lung fibrosis. *Arthritis Rheumatol* 2014;66: 714–725.
20. Karimizadeh E, Sharifi-Zarchi A, Nikaein H, Salehi S, Salamatian B, Elmi N, *et al.* Analysis of gene expression profiles and protein-protein interaction networks in multiple tissues of systemic sclerosis. *BMC Med Genomics* 2019;12:199.
21. Wang Y, Yella J, Chen J, McCormack FX, Madala SK, Jegga AG. Unsupervised gene expression analyses identify IPF-severity correlated signatures, associated genes and biomarkers. *BMC Pulm Med* 2017;17:133.
22. Hsu E, Shi H, Jordan RM, Lyons-Weiler J, Pilewski JM, Feghali-Bostwick CA. Lung tissues in patients with systemic sclerosis have gene expression patterns unique to pulmonary fibrosis and pulmonary hypertension. *Arthritis Rheum* 2011;63:783–794.
23. Biasin V, Marsh LM, Egemnazarov B, Wilhelm J, Ghanim B, Klepetko W, *et al.* Meprin β, a novel mediator of vascular remodelling underlying pulmonary hypertension. *J Pathol* 2014;233:7–17.
24. Maurer B, Busch N, Jüngel A, Pileckyte M, Gay RE, Michel BA, *et al.* Transcription factor Fos-related antigen-2 induces progressive peripheral vasculopathy in mice closely resembling human systemic sclerosis. *Circulation* 2009;120:2367–2376.
25. Reich N, Maurer B, Akhmetshina A, Venalis P, Dees C, Zerr P, *et al.* The transcription factor Fra-2 regulates the production of extracellular matrix in systemic sclerosis. *Arthritis Rheum* 2010;62:280–290.
26. Gao X, Jia G, Guttman A, DePianto DJ, Morshead KB, Sun KH, *et al.* Osteopontin links myeloid activation and disease progression in systemic sclerosis. *Cell Rep Med* 2020;1:100140.
27. Ando K, Nakashita T, Kaneko N, Takahashi K, Motojima S. Associations between peripheral blood eosinophil counts in patients with systemic sclerosis and disease severity. *Springerplus* 2016;5:1401.
28. Hoenerhoff MJ, Starost MF, Ward JM. Eosinophilic crystalline pneumonia as a major cause of death in 129S4/SvJae mice. *Vet Pathol* 2006;43: 682–688.
29. Matute-Bello G, Downey G, Moore BB, Groshong SD, Matthay MA, Slutsky AS, *et al.*; Acute Lung Injury in Animals Study Group. An official American Thoracic Society workshop report: features and measurements of experimental acute lung injury in animals. *Am J Respir Cell Mol Biol* 2011;44:725–738.
30. Angelidis I, Simon LM, Fernandez IE, Strunz M, Mayr CH, Greiffo FR, *et al.* An atlas of the aging lung mapped by single cell transcriptomics and deep tissue proteomics. *Nat Commun* 2019;10:963.
31. Tabula Muris C; Tabula Muris Consortium. A single-cell transcriptomic atlas characterizes ageing tissues in the mouse. *Nature* 2020;583: 590–595.
32. Tabula Muris Consortium; Overall coordination; Logistical coordination; Organ collection and processing; Library preparation and sequencing; Computational data analysis; Cell type annotation; Writing group; Supplemental text writing group; Principal investigators. Single-cell transcriptomics of 20 mouse organs creates a *Tabula Muris*. *Nature* 2018;562:367–372.
33. Naba A, Clauser KR, Ding H, Whittaker CA, Carr SA, Hynes RO. The extracellular matrix: tools and insights for the "omics" era. *Matrix Biol* 2016;49:10–24.
34. Morse C, Tabib T, Sembrat J, Buschur KL, Bittar HT, Valenzi E, *et al.* Proliferating SPP1/MERTK-expressing macrophages in idiopathic pulmonary fibrosis. *Eur Respir J* 2019;54:1802441.
35. Tian Y, Li H, Gao Y, Liu C, Qiu T, Wu H, *et al.* Quantitative proteomic characterization of lung tissue in idiopathic pulmonary fibrosis. *Clin Proteomics* 2019;16:6.
36. Åhrman E, Hallgren O, Malmström L, Hedström U, Malmström A, Bjermer L, *et al.* Quantitative proteomic characterization of the lung extracellular matrix in chronic obstructive pulmonary disease and idiopathic pulmonary fibrosis. *J Proteomics* 2018;189: 23–33.

37. Yu G, Ibarra GH, Kaminski N. Fibrosis: lessons from OMICS analyses of the human lung. *Matrix Biol* 2018;68-69:422–434.
38. Mariani TJ, Reed JJ, Shapiro SD. Expression profiling of the developing mouse lung: insights into the establishment of the extracellular matrix. *Am J Respir Cell Mol Biol* 2002;26:541–548.
39. Bradshaw AD, Sage EH. SPARC, a matricellular protein that functions in cellular differentiation and tissue response to injury. *J Clin Invest* 2001; 107:1049–1054.
40. Basu D, Reveille JD. Anti-scl-70. *Autoimmunity* 2005;38:65–72.
41. Cavagna L, Nuño L, Scirè CA, Govoni M, Longo FJL, Franceschini F, *et al.*; AENEAS (American, European NEtwork of Antisynthetase Syndrome) collaborative group. Clinical spectrum time course in anti Jo-1 positive antisynthetase syndrome: results from an international retrospective multicenter study. *Medicine (Baltimore)* 2015;94:e1144.
42. Mack MR, Brestoff JR, Berrien-Elliott MM, Trier AM, Yang TB, McCullen M, *et al.* Blood natural killer cell deficiency reveals an immunotherapy strategy for atopic dermatitis. *Sci Transl Med* 2020;12:eaay1005.
43. Ucero AC, Bakiri L, Roediger B, Suzuki M, Jimenez M, Mandal P, *et al.* Fra-2-expressing macrophages promote lung fibrosis in mice. *J Clin Invest* 2019;129:3293–3309.
44. Mesnil C, Raulier S, Paulissen G, Xiao X, Birrell MA, Pirottin D, *et al.* Lung-resident eosinophils represent a distinct regulatory eosinophil subset. *J Clin Invest* 2016;126:3279–3295.
45. Schnieder J, Mamazhakypov A, Birnhuber A, Wilhelm J, Kwapiszewska G, Ruppert C, *et al.* Loss of LRP1 promotes acquisition of contractile-myofibroblast phenotype and release of active TGF-β1 from ECM stores. *Matrix Biol* 2020;88:69–88.
46. Seidenberg J, Stellato M, Hukara A, Ludewig B, Klingel K, Distler O, *et al.* The AP-1 transcription factor Fosl-2 regulates autophagy in cardiac fibroblasts during myocardial fibrogenesis. *Int J Mol Sci* 2021;22:1861.
47. Tabib T, Huang M, Morse N, Papazoglou A, Behera R, Jia M, *et al.* Myofibroblast transcriptome indicates $SFRP2^{hi}$ fibroblast progenitors in systemic sclerosis skin. *Nat Commun* 2021;12:4384.
48. Joshi N, Watanabe S, Verma R, Jablonski RP, Chen CI, Cheresh P, *et al.* A spatially restricted fibrotic niche in pulmonary fibrosis is sustained by M-CSF/M-CSFR signalling in monocyte-derived alveolar macrophages. *Eur Respir J* 2020;55:1900646.
49. Jaffar J, Griffiths K, Oveissi S, Duan M, Foley M, Glaspole I, *et al.* $CXCR4^{+}$ cells are increased in lung tissue of patients with idiopathic pulmonary fibrosis. *Respir Res* 2020;21:221.
50. Baran CP, Opalek JM, McMaken S, Newland CA, O'Brien JM Jr, Hunter MG, *et al.* Important roles for macrophage colony-stimulating factor, CC chemokine ligand 2, and mononuclear phagocytes in the pathogenesis of pulmonary fibrosis. *Am J Respir Crit Care Med* 2007; 176:78–89.
51. Makino H, Aono Y, Azuma M, Kishi M, Yokota Y, Kinoshita K, *et al.* Antifibrotic effects of CXCR4 antagonist in bleomycin-induced pulmonary fibrosis in mice. *J Med Invest* 2013;60:127–137.
52. Birnhuber A, Biasin V, Schnoegl D, Marsh LM, Kwapiszewska G. Transcription factor Fra-2 and its emerging role in matrix deposition, proliferation and inflammation in chronic lung diseases. *Cell Signal* 2019;64:109408.
53. Abel AM, Yang C, Thakar MS, Malarkannan S. Natural killer cells: development, maturation, and clinical utilization. *Front Immunol* 2018;9:1869.
54. Schnoegl D, Hochgerner M, Gotthardt D, Marsh LM. Fra-2 is a dominant negative regulator of natural killer cell development. *Front Immunol* 2022;13:909270.
55. Poggi A, Zocchi MR. HIV-1 Tat triggers TGF-beta production and NK cell apoptosis that is prevented by pertussis toxin B. *Clin Dev Immunol* 2006;13:369–372.
56. Li Y, Bao J, Bian Y, Erben U, Wang P, Song K, *et al.* $S100A4^{+}$ macrophages are necessary for pulmonary fibrosis by activating lung fibroblasts. *Front Immunol* 2018;9:1776.
57. Landi C, Bargagli E, Carleo A, Refini RM, Bennett D, Bianchi L, *et al.* Bronchoalveolar lavage proteomic analysis in pulmonary fibrosis associated with systemic sclerosis: S100A6 and 14-3-3ε as potential biomarkers. *Rheumatology (Oxford)* 2019;58:165–178.
58. Liu W, Meridew JA, Aravamudhan A, Ligresti G, Tschumperlin DJ, Tan Q. Targeted regulation of fibroblast state by CRISPR-mediated CEBPA expression. *Respir Res* 2019;20:281.
59. Li X, Wang W, Wang J, Malovannaya A, Xi Y, Li W, *et al.* Proteomic analyses reveal distinct chromatin-associated and soluble transcription factor complexes. *Mol Syst Biol* 2015;11:775.
60. Maurer B, Reich N, Juengel A, Kriegsmann J, Gay RE, Schett G, *et al.* Fra-2 transgenic mice as a novel model of pulmonary hypertension associated with systemic sclerosis. *Ann Rheum Dis* 2012;71:1382–1387.
61. Ho KT, Reveille JD. The clinical relevance of autoantibodies in scleroderma. *Arthritis Res Ther* 2003;5:80–93.
62. Galindo-Feria AS, Notarnicola A, Lundberg IE, Horuluoglu B. Aminoacyl-tRNA synthetases: on anti-synthetase syndrome and beyond. *Front Immunol* 2022;13:866087.
63. Parker JM, Glaspole IN, Lancaster LH, Haddad TJ, She D, Roseti SL, *et al.* A phase 2 randomized controlled study of tralokinumab in subjects with idiopathic pulmonary fibrosis. *Am J Respir Crit Care Med* 2018;197:94–103.
64. Maher TM, Costabel U, Glassberg MK, Kondoh Y, Ogura T, Scholand MB, *et al.* Phase 2 trial to assess lebrikizumab in patients with idiopathic pulmonary fibrosis. *Eur Respir J* 2021;57:1902442.
65. Raghu G, Richeldi L, Crestani B, Wung P, Bejuit R, Esperet C, *et al.* SAR156597 in idiopathic pulmonary fibrosis: a phase 2 placebo-controlled study (DRI11772). *Eur Respir J* 2018;52:1801130.
66. Gabrielli A, Avvedimento EV, Krieg T. Scleroderma. *N Engl J Med* 2009; 360:1989–2003.
67. Heukels P, Moor CC, von der Thüsen JH, Wijsenbeek MS, Kool M. Inflammation and immunity in IPF pathogenesis and treatment. *Respir Med* 2019;147:79–91.
68. Huang J, Maier C, Zhang Y, Soare A, Dees C, Beyer C, *et al.* Nintedanib inhibits macrophage activation and ameliorates vascular and fibrotic manifestations in the Fra2 mouse model of systemic sclerosis. *Ann Rheum Dis* 2017;76:1941–1948.